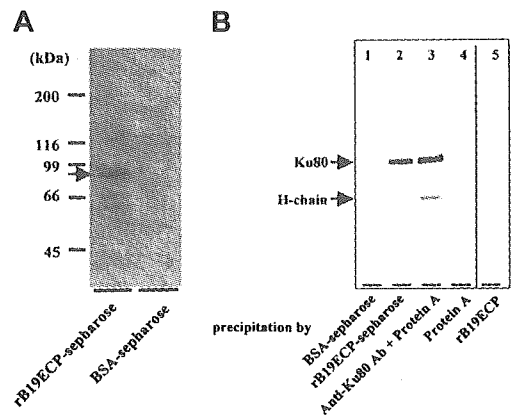rB19ECP. Confocal miscroscopy analysis was performed with a D-ECLIPSE CI (Nikon, Kawasaki, Japan) mounted with 20×/0.50 or 40×/0.75 Plan Fluor dry objective lenses. Excitation at 488 nm from an argon laser and at 543 nm from a helium-neon laser was used. Images were acquired with E2-CI 2.00 software (Nikon) and processed with Adobe Photoshop 7.0.1 (Adobe Systems, San Jose, CA).

Results

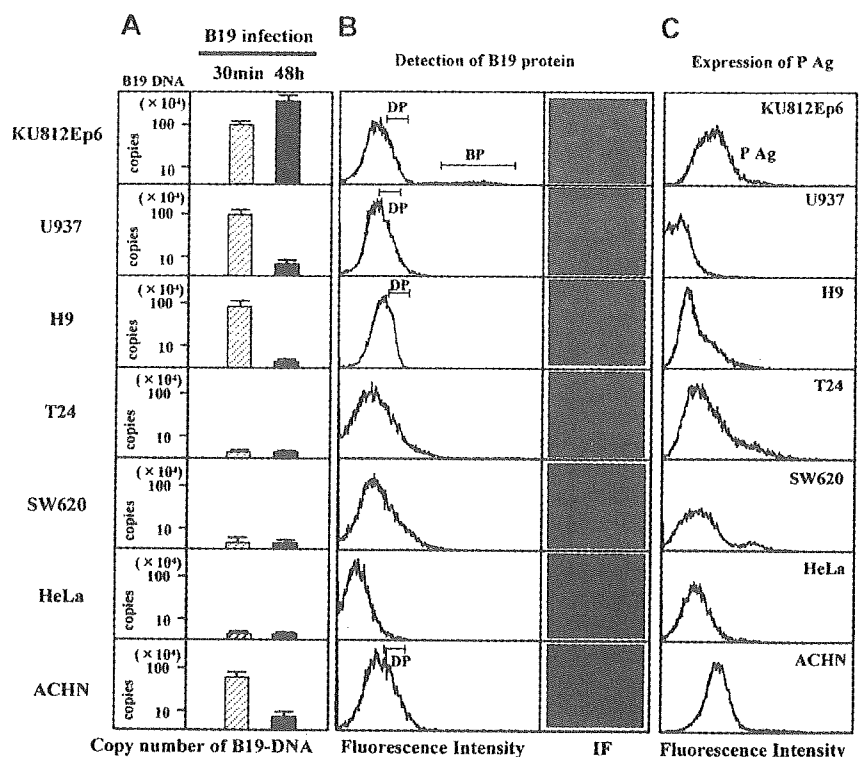### Identification of B19-binding protein on the cell surface of nonerythroid cells

To identify a putative receptor for B19, we first checked the expression of P antigen (Figure 1). Flow cytometry analysis revealed that α5β1 integrin[6] was also positive on the surface of all cell lines tested (data not shown). We then studied the binding and replication of B19 in association with the expression of P antigen and α5β1 integrin. Quantitative study for cell-surface binding, B19 DNA replication, and fluorescence-activating cell sorting (FACS) analysis using anti–B19 protein (VP2) antibody PAR3 revealed that B19 binds not only to a P antigen–expressing erythroid cell line KU812Ep6 but also to a macrophage cell line, U937, to a T-cell line, H9, and a renal carcinoma cell line, ACHN, in which P antigen was undetectable on the cell surface. None of the cell lines, T24, SW620, and HeLa, bound B19 despite surface P antigen expression (left column in Figure 1A). FACS analysis at 48 hours after B19 infection revealed 2 types of staining patterns for B19 protein following immunohistochemistry using PAR3: (1) intense staining in KU812Ep6 and (2) weak staining in Ku812Ep6, U937, H9, and ACHN (left column in Figure 1B). Replication of B19 DNA and the synthesis of B19 protein was observed in KU812Ep6, but not in any of the other cells, irrespective of the presence of P antigen (right column in Figure 1A and right column in Figure 1B) or α5β1 integrin.

Figure 2. Determination of B19-binding protein on surface of T cell line H9. (A) Isolation of B19-binding protein from H9 surface. Surface proteins H9 of cells were biotinylated. Cell lysate from 1 × 10¹¹ biotinylated H9 cells was mixed with rB19ECP-conjugated Sepharose or with BSA-conjugated Sepharose. Precipitated protein was isolated and reacted with streptavidin–horseradish-peroxidase conjugate on PVDF membranes, followed by the chemiluminescence detection. (B) Western blotting of protein from H9 surface with anti-Ku80 antibody. Lanes 1-4 show cell lysate precipitated with indicated protein or protein-conjugated Sepharose. Lane 5 shows the rB19ECP (1 μg) resolved by electrophoresis under denaturing conditions.
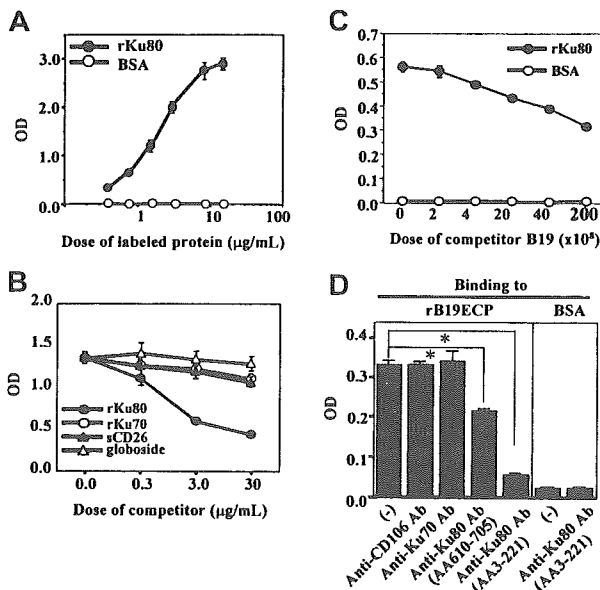
To determine the cell-surface molecule responsible for B19 binding to H9 cells, a recombinant empty capsid protein of B19 (rB19ECP) was used. Biotinylated rB19ECP bound H9 in a dose-dependent manner (data not shown). We then purified the rB19ECP-binding molecule from the cell surface of H9 using rB19ECP-conjugated Sepharose (rB19ECP-Sepharose). The precipitated 80-kDa protein (Figure 2A) was analyzed by matrix-assisted laser desorption ionization-time of flight mass spectrometry. The obtained data were collated and submitted for homology search using the Swiss Prot and NCB Inr databases. The Ku80 autoantigen was identified as the gene product with the highest

Figure 1. B19 infectivity and expression of P antigen. Each cell line (2 × 10⁶) was inoculated with B19 (1 × 10¹¹ copies of B19 DNA) for 30 minutes at 4°C and washed with PBS, pH 7.2, 3 times. Half of the cells in each group were used for evaluation of B19 adsorption (left column in panel A), and remaining cells in 3 mL RPMI containing 10% FBS were further incubated at 37°C for 48 hours to measure B19 DNA replication (right column in panel A) or to detect B19 protein (B). (A) B19 binding and replication of B19 in various cell lines. B19-infected cells were quantified for B19 DNA as described in "Materials and methods." The left column (▨) is regarded as B19 adsorption, and the right column (▬) as B19 replication. The scale for B19 DNA is shown in logarithm. (B) Detection of B19 protein in B19-infected cells. After a 48-hour incubation with B19, the cells were washed 3 times with PBS and they were fixed with 4% paraformaldehyde followed by permeabilization with SAP buffer (0.1% saponin, 0.05% NaN₃ in Hanks balanced salt solution). Then, cells were incubated with PAR3 at a concentration of 5 μg/mL on ice for 30 minutes, followed by an incubation with FITC-conjugated goat anti–mouse IgG. The expression of B19 protein in cytoplasm was analyzed by flow cytometry with PAR3 (line) or isotype-matched antibody 1F5 (shadow; left panel), or by immunofluorescence (IF) staining with PAR3 (right panel). Two types of positive patterns were observed in flow cytometry: dull positive (DP) pattern in KU812Ep6, U937, H9, and ACHN; bright positive (BP) pattern in KU812Ep6. (C) Flow cytometry analysis of P antigen expression on the cell surface. Indicated cells were incubated with antigloboside antibody, GL4, followed by PE-labeled anti–rabbit IgG. Shadow represents staining using rabbit IgG as a negative control.
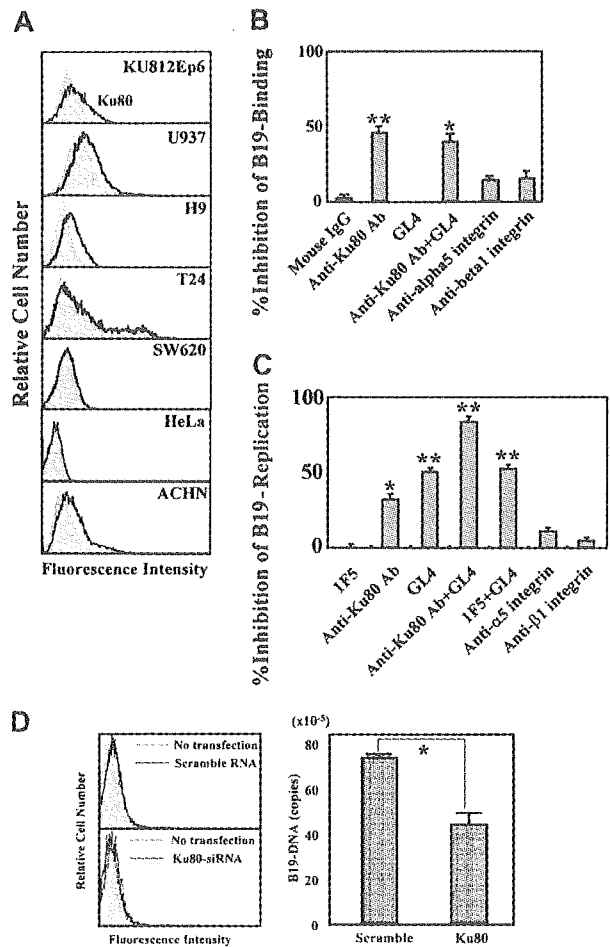
homology in both databases. As a confirmation, the rB19ECP-binding 80-kDa protein reacted with anti-Ku80 antibody (Figure 2B). Competitive ELISA further confirmed the specific binding between Ku80 and B19. Biotinylated recombinant Ku80 (rKu80) reacted with rB19ECP fixed to microwells (Figure 3A); the binding was selectively inhibited by unlabeled rKu80 but not by recombinant Ku70 (rKu70), globoside, or recombinant soluble CD26 (sCD26)[23] (Figure 3B). This binding was also inhibited in the presence of native B19 particles from infected patients (Figure 3C). Two anti-Ku80 antibodies significantly inhibited the binding of biotinylated rKu80 and rB19ECP, whereas anti-Ku70 antibody or anti-CD106 antibody failed to inhibit the binding (Figure 3D).

Ku80 participates in B19 binding and subsequent entry

We next investigated whether Ku80 would participate in B19 binding on the cell surface and facilitate B19 entry. KU812Ep6, U937, H9, and ACHN cells efficiently bound B19 (Figure 1A) and all of these cells clearly expressed Ku80 on their surface (Figure 4A). On the other hand, Ku80 was undetectable on T24, SW620, and HeLa cells, and no binding of B19 occurred (Figures 4A and 1A). An in vitro infection experiment demonstrated efficient replication of B19 DNA in KU812Ep6 cells that expressed both Ku80 and P antigen. B19 failed to amplify itself in U937, H9, and ACHN cells, which express Ku80 but no detectable levels of P antigen on the cell surface (Figures 1 and 4A). T24, SW620, and HeLa cells were nonpermissive for B19 infection although they expressed P antigen (Figure 1) and α5β1 integrin.

Figure 4. Role of Ku80 in B19 infection in vitro. (A) Ku80 expression on cell surface. The indicated cell lines were reacted with 5 μg/mL mouse monoclonal anti-Ku80 antibody (line) or 5 μg/mL isotype-matched mouse monoclonal antibody 1F5 (shadow), followed by FITC-labeled anti–mouse IgG antibodies. Cells were washed with PBS, and cell-surface expression of Ku80 was analyzed by flow cytometry. (B) Blocking of B19 adsorption by anti-Ku80 antibody or antigloboside antibody. KU812Ep6 cells (2 × 10 [6]) were infected with B19 (2 × 10^{11} copies of B19 DNA) on ice for 30 minutes in the presence of the indicated antibodies (5 μg/mL) and extensively washed with PBS 3 times. To activate α5β1 integrin, anti-integrin antibodies were used in the presence of divalent ions (1 mM Mn^{2+}, 1 mM Mg^{2+}). B19 DNA in each group was quantified by quantitative PCR. The blocking ability of B19 binding by each antibody was expressed as percent decrease of B19-DNA in each group compared to that in antibody-untreated cells. **$P < .01$, *$P < .05$ by Student t test. (C) Blocking of B19 replication by anti-Ku80 antibody or antigloboside antibody. KU812Ep6 cells were infected with B19 and washed as described. Cells were further incubated for 48 hours at 37°C and washed with PBS 3 times before the quantitative study of B19 DNA. To activate α5β1 integrin, anti-integrin antibodies were used in the presence of divalent ions (1 mM Mn^{2+}, 1 mM Mg^{2+}). The blocking ability of B19 replication by each antibody was expressed as described. **$P < .01$, *$P < .05$ by Student t test. (D) RNA interference of Ku80 in KU812Ep6 cells. Cell-surface expression of Ku80 was examined by flow cytometry in scramble RNA or siRNA of Ku80-transfected KU812Ep6 cells (left panel). KU812Ep6 cells treated with indicated RNA were reacted with 5 μg/mL mouse monoclonal anti-Ku80 antibody or 5 μg/mL isotype-matched mouse monoclonal antibody 1F5 (shadow), followed by FITC-labeled anti–mouse IgG antibodies. B19 association of siRNA-transfected KU812Ep6 cells was evaluated by quantitative PCR (right panel). Sample DNA was prepared from extensively washed scramble RNA or siRNA of Ku80-transfected KU812Ep6 cells after 2 hours of incubation with B19. *$P < .01$ by Student t test.


Figure 3. Specific binding of rB19ECP to Ku80. (A) Specific binding of Ku80 to rB19ECP. Indicated concentration of biotinylated rKu80 or biotinylated BSA was reacted with rB19ECP fixed to 96 microwells and detected by ELISA. (B) Competitive ELISA for rB19ECP binding to rKu80. Biotinylated rKu80 (2 μg/mL) was reacted with rB19ECP fixed to wells in the presence of indicated doses of unlabeled rKu80, rKu70, sCD26, or globoside. (C) Inhibition of rB19ECP binding to rKu80 by purified B19. Biotinylated rKu80 (1 μg/mL) was added to rB19ECP fixed to wells in the presence of B19 that was purified from B19+ serum with repeated microfiltration. Doses of B19 are expressed as copy numbers of B19 DNA. (D) Inhibition of rB19ECP binding to rKu80 by anti-Ku80 antibodies. Binding of biotinylated rKu80 or biotinylated BSA to rB19ECP fixed to wells was measured in the presence of isotype-matched mouse monoclonal antibodies as indicated.

Ku80 functions as a coreceptor for B19 infection together with P antigen

We then performed an inhibition test for B19 infection of KU812Ep6 cells using antibodies against Ku80, P antigen, α5β1 integrin. Anti-Ku80 antibody inhibited B19 binding, whereas anti-P antibody, GL4, did not inhibit B19 binding. Anti–α5 and anti–β1
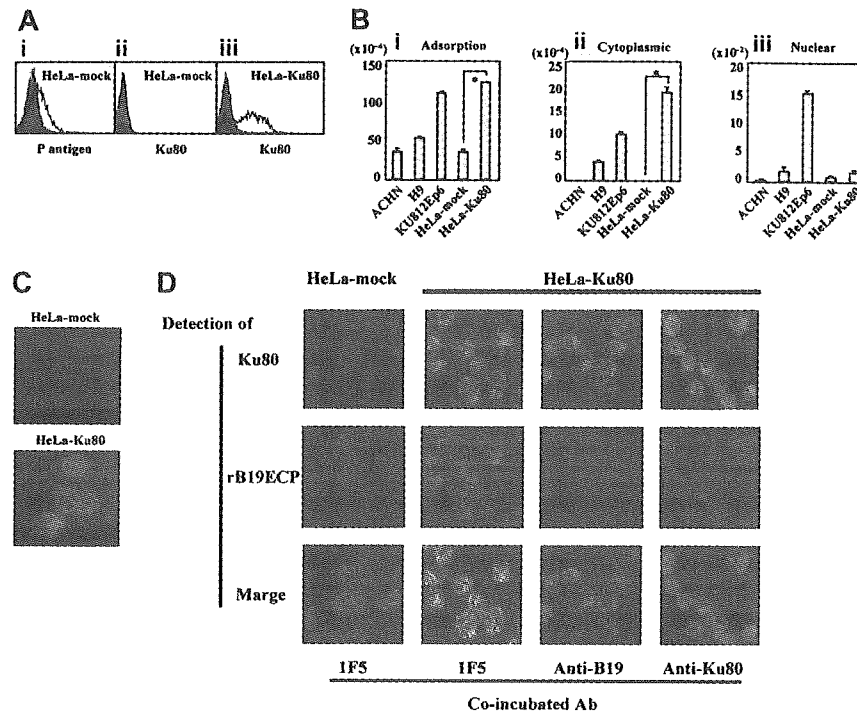
Figure 5. Transfection of Ku80 to HeLa cells. (A) Expression of Ku80 on HeLa cells transfected with pKu80. Ku80 cDNA was inserted to expression plasmid pcD and the resulted pKu80 was transfected to HeLa cells (HeLa-Ku80) using lipofectin. Empty pcD was used for a mock transfection (HeLa-mock). The transfected cells (2 × 10⁵) were incubated with 5 μg/mL of each antibody, anti-Ku80 antibody (ii,iii), GL4 (A1), or isotype-matched mouse monoclonal antibodies or rabbit serum (shadow), and then analyzed for the expression of P antigen or Ku80 on the cell surface. Figures show HeLa-mock expressed P antigen but not Ku antigen on the surface (i,ii), whereas HeLa-Ku80 expressed Ku80 (iii). (B) Increased binding and viral entry of B19 in HeLa-Ku80. The indicated cells (6 × 10⁵) were infected with B19 (2 × 10¹¹ copies of B19 DNA) for 30 minutes on ice. After washing cells 3 times with PBS, pH 7.2, DNA was extracted from 2 × 10⁵ cells. Remaining cells were further incubated for 30 minutes at 37°C. After washing cells 3 times with PBS, pH 4.5, a cytoplasmic and nuclear fraction was prepared, and then DNA was extracted from each fraction. Prepared DNA was subjected to a quantitative PCR to quantify B19 DNA. *$P < .01$ by Student t test. (C) B19 infection to HeLa-Ku80. HeLa-mock or HeLa-Ku80 cells (2 × 10⁵) were infected with B19 (2 × 10¹¹ copies of B19 DNA) for 30 minutes at 37°C. After being washed 3 times with PBS, cells were collected with 5 mM EDTA-PBS, pH 7.2, fixed with 4% paraformaldehyde and reacted with PAR3, followed by FITC-labeled anti–mouse IgG antibody as a secondary antibody. Thus prepared cells were then subjected to a confocal microscope analysis. The panel represents B19 entered into HeLa-Ku80. (D) Colocalization of rB19ECP and Ku80. HeLa-mock or HeLa-Ku80 (2 × 10⁵) cells were incubated with biotinylated rB19ECP (1 μg/mL) in the presence of 5 μg/mL inhibitor antibody indicated for 30 minutes at 37°C. After being washed 3 times with PBS, pH 7.2, cells were collected with 5 mM EDTA-PBS, and rB19ECP or Ku80 was detected by confocal microscopy analysis. Ku80 was detected by anti-Ku80 antibody followed by TRITC-labeled anti–mouse IgG antibody as a secondary antibody. Detection of biotinylated rB19ECP was done by avidin-FITC as described in "Materials and methods."
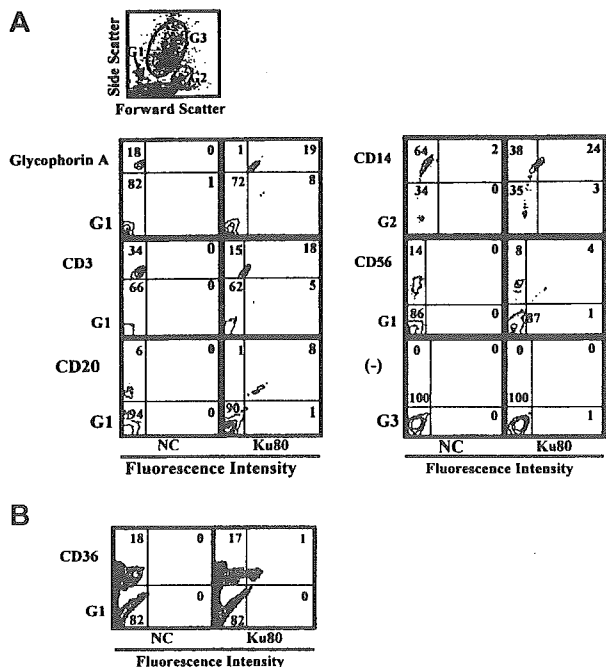
integrin antibodies caused a slight inhibition of B19 binding (Figure 4B). Both anti-Ku80 antibody and GL4 also inhibited B19 replication in KU812Ep6 cells. The simultaneous presence of both antibodies more strongly inhibited the replication of B19 DNA (Figure 4C). Presence of anti–α5 and anti–β1 integrin antibodies caused only a slight inhibition of B19 replication (Figure 4C). In other experiments, KU812Ep6 cells were treated with siRNA against Ku80 and then tested for the replication of B19 at B19 infection study. The results revealed the suppression of B19 binding to the KU812Ep6 cells with reduced expression of Ku80 (Figure 4D).

The role of Ku80 as a coreceptor for B19 infection was also supported by a transfection experiment using HeLa cells that were nonpermissive for B19 infection. Figure 5A shows that the surface of Ku80-transfected HeLa cells (HeLa-Ku80) became positive for Ku80 expression and binding of B19 to the cells was significantly enhanced (Figure 5B). Quantitative analysis of B19 DNA (Figure 5B) and confocal laser microscopy (Figure 5C) confirmed that B19 DNA and B19 protein were present in the cytoplasmic fraction of HeLa-Ku80 cells 30 minutes after infection, similar to Ku812Ep6. Furthermore, a coincubation experiment of rB19ECP and HeLa-Ku80 revealed the colocalization of rB19ECP and Ku80 in the cytoplasm or membrane (or both) of HeLa-Ku80 (Figure 5D). Moreover, association of rB19ECP and HeLa-Ku80 was apparently

inhibited by the presence of anti-B19 antibody or anti-Ku80 antibody (Figure 5D).

Ku80 is expressed on the surface of bone marrow cells

Because Ku80 is known as a nuclear protein, it is important to determine whether or not Ku80 is expressed on the cell-surface in vivo. Ku80 was not detected on the cell surface of peripheral blood mononuclear cells (data not shown). We then examined cell-surface expression of Ku80 in bone marrow cells because bone marrow cells are potential targets of B19 infection. Flow cytometry analysis of bone marrow cells demonstrated that Ku80 was highly expressed on the cell surface of erythroid progenitor cells expressing glycophorin A as well as on the surface of immune cells such as CD20⁺, CD3⁺, or CD14⁺ cells in bone marrow (Figure 6A). A small portion (5.6%) of CD36⁺ bone marrow cells, which may be permissive to B19 infection,[23] were also positive for the expression of Ku80 on the cell surface (Figure 6B). B19 binding to bone marrow cells was inhibited in the presence of anti-Ku80 antibody at B19 infection in vitro (data not shown). Figure 7 shows that the replication of B19 in bone marrow cells was significantly inhibited in the presence of anti-Ku80 antibody or GL4. The inhibition rate of B19 replication in the presence of both anti-Ku80 antibody and GL4 was similar to that in the presence of GL4.

A

Glycophorin A

CD14

CD3

CD56

CD20

G1

NC   Ku80
Fluorescence Intensity

NC   Ku80
Fluorescence Intensity

B

CD36

G1

NC   Ku80
Fluorescence Intensity

Figure 6. Cell-surface expression of Ku80 in human bone marrow cells. Flow cytometry analysis of Ku80 expression on the cell surface. Bone marrow cells were reacted with indicated antibodies and anti-Ku80 antibody as described in "Materials and methods," and then the expression of surface molecules was analyzed. Prior to the study, each sample had been analyzed by the scattered plot. The results showed that the glycophorin A+, CD3+, CD20+, CD56+, or CD36+ cells were scattered in gate 1 (G1), and CD14+ cells in gate 2 (G2),'and that there were no glycophorin A+, CD3+, CD20+, CD56+, or CD36+ cells in gate 3 (G3). Then the expression of Ku80 on cell surface in gated cells was analyzed. The gate used in each experiment is shown at left-lower side of each plot. (A) Gates used in the experiment and detection of Ku80 on the surface of various cell lineages. (B) Detection of Ku80 on the surface of CD36+ bone marrow cells.

Discussion

The presented data implicate Ku80 as a coreceptor involved in B19 infection. U937, H9, and ACHN cells expressing Ku80 showed B19 binding, but some cells with P antigen failed to bind B19 unless these cells expressed Ku80 on their surface. A marked increase in B19 binding in Ku80-transfected HeLa cells and the inhibition of B19 infectivity by anti-Ku80 antibody or siRNA to Ku80 suggests a Ku80-dependent B19 interaction with the targeted cells. Specific inhibition of B19 binding by anti-Ku80 antibody that recognized the N-terminus of the Ku80 protein suggests that B19 interacts with specific sites of Ku80 on the cell surface. Further, Epstein-Barr virus or hepatitis virus C failed to bind either to Ku80-expressing HeLa or U937 cells (data not shown). These results suggest that Ku80 is one of the specific receptors for B19 infection.

Ku is a heterodimeric DNA-binding protein consisting of a 70-kDa (Ku70) and an 80-kDa (Ku80) subunit and was originally identified as a nuclear antigen recognized by autoantibodies in patients with systemic lupus erythematosus and scleroderma.[25] Ku has a central role in multiple nuclear processes, including DNA repair, chromosome maintenance, transcription regulation, and V(D)J recombination. Ku is abundant in the nucleus, consistent with its function as a DNA-protein kinase (DNA-PK).[26,27] However, recent studies have shown cytoplasm or surface localization of Ku in various types of cells, including of leukemia, multiple myeloma, and tumor cell lines. Ku is a component of the DNA-PK

complex in membrane rafts of mammalian cells.[26] Although the role of surface Ku80 has not been well clarified,[28] signal transduction and Ku80 are coupled in both B and T cells,[25,28,29] and localization of the DNA-PK complex in lipid rafts suggests a putative role in the signal transduction pathway following ionizing radiation.[26] It was recently reported that Ku interacts with metalloproteinase 9 at the cell surface of highly invasive hematopoietic cells of normal and tumor cell origin, and Ku80/MMP-9 interaction at the cell membrane may result in contribution to the invasion of tumor cells through regulation of extracellular matrix remodelling.[30] Further, the membrane form of Ku, whose expression is induced at hypoxia, mediates cell adhesion of plasma cells,[30-32] indicating a role for Ku as an adhesion receptor for fibronectin.[33] The present study showed that Ku80 is positive on the surface of CD3+ cells, CD20+ cells, CD14+ cells, glycophorin A+ cells, and CD36+ cells from bone marrow where B19 infection is permissive.

We have discovered a novel role of Ku80 as a cellular receptor in B19 infection. Anti-Ku80 antibody, however, did not cause complete inhibition of B19 infection, whereas pretreatment with anti-Ku80 antibody together with GL4 strongly inhibited B19 infectivity in KU812Ep6 cells and human bone marrow cells, showing the necessity of P antigen as a receptor. A recent report showed that $\alpha5\beta1$ integrin has a role in B19 entry into host cells,[6] and KU812Ep6, U937, H9, ACHN, and HeLa cells all expressed $\alpha5\beta1$ integrin on their surface (data not shown). However, B19 entry into U937- and H9-expressing Ku80 and $\alpha5\beta1$ integrin or HeLa cells with P antigen and $\alpha5\beta1$ integrin was insufficient or negative (Figures 1 and 5B). B19 entry was marked in KU812Ep6 cells or Ku80-HeLa cells that expressed Ku80, P antigen, and $\alpha5\beta1$ integrin on their surface, showing the necessity of P antigen for efficient binding and the virus entry afterward. Anti–$\alpha5$ and anti–$\beta1$ integrin antibodies, which inhibited the entry of B19 into K562 cells,[6] caused a slight inhibition of B19 binding as well as B19 replication in KU812Ep6, supporting the participation of $\alpha5\beta1$ integrin in B19 infection. We are currently investigating the precise mechanism of the interaction among B19-related receptors such as P antigen, Ku80, and $\alpha5\beta1$ integrin in association with the following signal transduction in B19-infected cells.

The use of multiple receptors for entry into cells has been observed frequently in virus infection, such as by α herpesviruses, HHV-8 or HIV.[34,35] We have shown that B19 uses at least 2 receptors, Ku80 and P antigen, in the process of infection. Ku80

Antibodies added at B19 infection
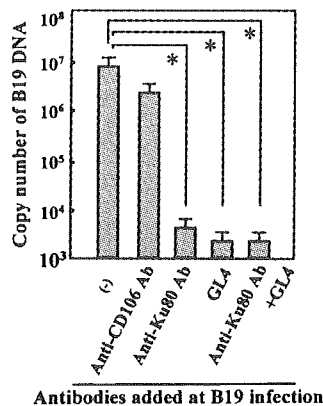
Figure 7. Blocking of B19 infection of bone marrow cells by anti-Ku80 antibody or antigloboside antibody. Bone marrow cells (2 × 10^{6}) were infected with B19 (2 × 10^{11} copies of B19 DNA) with the indicated antibodies and evaluated for quantity of B19 DNA as described. Anti-CD106 antibody was a mouse monoclonal antibody used as a negative control. The differences in the results between control (−) and other samples were statistically analyzed. *P < .01 by Student t test.

may function as an efficient B19-capturing molecule on the cell surface and may also contribute to B19 entry into cells; markedly enhanced entry of B19 in Ku80-HeLa cells (Figure 5C-D) suggests that Ku80 mediates efficient B19 entry in cooperation with P antigen and probably with α5β1 integrin.[6] Although Ku80 can interact with Epstein-Barr virus protein in the nucleus,[36] this study is the first to show the use of Ku80 antigen as a cellular receptor for virus infection. Despite marked entry of B19, synthesis of B19 protein was unsuccessful in Ku80-HeLa cells, but was possible only in erythroid cell lines, indicating that unknown intracellular factors may be required for B19 replication in the targeted cells.[37,38]

Ku80 is not found in circulating mononuclear cells from healthy volunteers but is positive on the surface of B19-binding cells in vivo, such as immune cells in tonsils, erythroblasts, T cells, B cells, macrophages in bone marrow, and immune cells including follicular dendritic cells in rheumatoid joints, indicating the surface expression of Ku antigen may be restricted by environmental conditions. Of interest is that the oxygen levels are markedly low in bone marrow and joints[39-41] compared with that in blood, and surface Ku80 is inducible with hypoxia.[31,32] A recent study suggests the efficiency of B19 infection increases with hypoxia.[42] These studies suggest that surface Ku80 induced with hypoxia may participate in the process of B19 infection of joints and bone marrow.

Ku80 expression on the surface of immune cells in bone marrow in vivo may explain clinical findings associated with B19 infection to nonerythroid cells. Namely, B19 infection often causes a decreased number of leukocytes or lymphocytes in blood during acute B19 infection, as well as increased levels of TNF-α and IFN-γ in blood or rheumatoid joints, and the detection of B19 on T cells, B cells, or macrophages in tonsils, bone marrow, or rheumatoid joints. B19 may infect immune cells in bone marrow or the synovium and persist to lead to secrete an inflammatory cytokine through the activation of AP1 and AP2 by B19 NS1.[43] Stimulation of cellular receptors with B19 may trigger activation of signal cascades in host cells, which may explain why immune cells in acute and prolonged B19 infection or in the joints of rheumatoid arthritis are functionally altered.

Acknowledgments

References

1. Anderson MJ, Jones SE, Fisher-Hoch SP, et al. Human parvovirus, the cause of erythema infectinosum (fifth disease) [letter]? Lancet. 1983;1:1387.

2. Brown KE, Young NS. Parvovirus B19 in human disease. Annu Rev Med. 1997;48:59-67.

3. Brown KE, Anderson SM, Young NS. Erythrocyte P antigen: cellular receptor for B19 parvovirus. Science. 1993;262:114-117.

4. Weigel-Kelly KA, Yoder MC, Srivastava A. Recombinant human parvovirus B19 vectors: erythrocyte P antigen is necessary but not sufficient for successful transduction of human hematopoietic cells. J Virol. 2001;75:4110-4116.

5. Kaufmann B, Baxa U, Chipman PR, Rossmann MG, Modrow S, Seckler R. Parvovirus B19 does not bind to membrane-associated globoside in vitro. Virology. 2005;332:189-198.

6. Weigel-Kelley KA, Yoder MC, Srivastava A. α5β1 integrin as a cellular co-receptor for human parvovirus B19: requirement of functional activation of {beta} 1 integrin for viral entry. Blood. 2003; 102:3927-3933.

7. Wagner AD, Goronzy JJ, Matteson EL, Weyand CM. Systemic monocyte and T cell activation in a patient with human parvovirus B19 infection. Mayo Clin Proc. 1995;70:261-265.

8. Murai C, Munakata Y, Takahashi Y, et al. Rheumatoid arthritis after human parvovirus B19 infection. Ann Rheum Dis. 1999;58:130-132.

9. Anderson MJ, Higgins PG, Davis LR, et al. Experimental parvovirus infection in humans. J Infect Dis. 1985;152:257-265.

10. Barlow GD, Mckendrick MW. Parvovirus B19 causing leucopenia and neutropenia in a healthy adult. J Infect. 2000;40:192-195.

11. Nesher G, Osborn TG, Moore TL. Parvovirus infection mimicking systemic lupus erythematosus. Semin Arthritis Rheum. 1995;24:297-303.

12. Kerr JR, Barah F, Mattey DL, et al. Circulating tumor necrosis factor-α and interferon-γ are detectable during acute and convalent parvovirus B19 infection and are associated with prolonged and chronic fatigue. J Gen Virol. 2001;82:3011-3019.

13. Soderlund M. Persistence of parvovirus B19 DNA in synovial membranes of young patients with and without chronic arthropathy. Lancet. 1997; 349:1063-1065.

14. Takahashi Y, Murai C, Munakata Y, et al. Human parvovirus B19 as a causative agent for rheumatoid arthritis. Proc Natl Acad Sci U S A. 1998;95: 8227-8232.

15. Miyagawa E, Yoshida T, Takahashi H, et al. Infection of the erythroid cell line, KU812Ep6 with human parvovirus B19 and its application to titration of B19 infectivity. J Virol Methods. 1999;83:45-54.

16. Saito T, Munakata Y, Fu Y, et al. Evaluation of anti-parvovirus B19 activity in sera by assay using quantitative polymerase chain reaction. J Virol Methods. 2003;107:81-87.

17. Yamaguchi K, Miyagawa E, Dan M, Miyazaki T, Ikeda H. Cellulose hollowfibers (BMMS) used in the filter membrane can trap human parvovirus B19 [abstract]. Electron Microsc. 2002;2:115.

18. Kajigaya S, Shimada T, Fujita S, Young NS. Self-assembled B19 parvovirus capsids, produced in a baculovirus system, are antigenically and immunogenically similar to native virions. Proc Natl Acad Sci U S A. 1991;88:4646-4650.

19. Yaegashi N, Tada K, Shiraishi H, Ishii T, Nagata K, Sugamura K. Characterization of monoclonal antibodies against human parvovirus B19. Microbiol Immunol. 1989;33:561-567.

20. Brown CS, Jensen T, Meloen RH, et al. Localization of an immunodominant domain on baculovirus produced parvovirus B19 capsids: correlation to a major surface region on the native virus particle. J Virol. 1992;66:6989-6996.

21. Harata N, Sasaki T, Osaki H, et al. Therapeutic treatment of New Zealand mouse disease by a limited number of anti-idiotypic antibodies conjugated with neocarzinostatin. J Clin Invest. 1990; 86:769-776.

22. Okayama H, Berg P. A cDNA cloning vector that permits expression of cDNA inserts in mammalian cells. Mol Cell Biol. 1983;3:280-289.

23. Tanaka T, Duke-Cohen JS, Kameoka J, et al. Enhancement of antigen-induced T-cell proliferation by soluble CD26/dispetidyl peptidase IV. Proc Natl Acad Sci U S A. 1994;91:3082-3086.

24. Morey AL, Fleming KA. Immunophenotyping of fetal haematopoietic cells permissive for human parvovirus B19 replication in vitro. Br J Haematol. 1992;82:302-309.

25. Mimori T, Ohosone Y, Hama N, et al. Isolation and characterization of cDNA encoding the 80-kDa subunit protein of the human autoantigen Ku(p70/p80) recognized by autoantibodies from patients with scleroderma-polymyositis overlap syndrome. Proc Natl Acad Sci U S A. 1990;87: 1777-1781.

26. Adam L, Bandyopadhyay D, Kumar R. Interferon-α signaling promotes nucleus-to-cytoplasmic redistribution of p95Vav, and formation of a multisubunit complex involving Vav, Ku80, and Trk-2. Biochem Biophys Res Commun. 2000;267:692-696.

27. Hector L, Darren G, Guillermo ET. Novel localization of the DNA-PK complex in lipid rafts. J Biol Chem. 2003;278:22136-22143.

28. Prabhakar BS, Allaway GP, Srinivasappa J, Notkins AL. Cell surface expression of the 70-kD component of Ku, a DNA-binding nuclear autoantigen. J Clin Invest. 1990;86:1301-1305.

29. Morio T, Hanissian SH, Bacharier LB, et al. Ku in the cytoplasm associates with CD40 in human B cells and translocates into the nucleus following incubation with IL-4 and anti-CD40 mAb. Immunity. 1999;11:339-348.

30. Monferran S, Paupert J, Dauvillier S, Salles B, Muller C. The membrane form of the DNA repair protein Ku interacts at the cell surface with metalloproteinase 9. EMBO J. 2004;23:3758-3768.

31. Teoh G, Urashima M, Greenfield EA, et al. The 86-kD subunit of Ku autoantigen mediates homotypic and heterotypic adhesion of multiple myeloma cells. J Clin Invest. 1998;101:1379-1388.

32. Lynch EM, Moreland RB, Ginis I, Perrine SP, Faller DV. Hypoxia-activated ligand HAL1/13 is lupus autoantigen Ku80 and mediates lymphoid cell adhesion in vitro. Am J Physiol Cell Physiol. 2001;280:897-911.

33. Sylvie M, Catherine M, Lionel M, Philippe F, Bernard S. The membrane-associated form of the DNA repair protein Ku is involved in cell

adhesion to fibronectin. J Mol Biol. 2004;26: 503-511.

34. Spear PG, Eisenberg RJ, Cohen GH. Three classes of cell surface receptors for alphaherpesvirus entry. Virology. 2000;275:1-8.

35. Shaw MA, Naranatt PP, Fu ZW, Bala C. Integrin α3β1(CD49c/29) is a cellular receptor for Kaposi's sarcoma-associated herpesvirus (KSHV/HHV-8) entry into the T cells. Cell. 2002;108:407-419.

36. Shieh B, Schultz J, Guinness M, Lacy J. Regulation of the human IgE receptor (Fc epsilonRIII/CD23) by Epstein-Barr virus (EBV): Ku autoantigen binds specifically to an EBV-responsive enhancer of CD23. Int Immunol. 1997;9:1885-1895.

37. Liu JM, Green SW, Shimada T, Young NS. A block in full-length transcript maturation in cells nonpermissive for B19 parvovirus. J Virol. 1992;66: 4686-4692.

38. Brunstein J, Soderlund VM, Hedman K. Identification of a novel splicing pattern as a basis of restricted tropism of erythrovirus B19. Virology. 2000;274: 284-291.

39. Bodamyali T, Stevens CR, Billingham MEJ, Ohta S, Blake DR. Influence of hypoxia in inflammatory synovitis. Ann Rheum Dis. 1998;57: 703-710.

40. Harrison SJ, Rameshwer P, Chang V, Bandari P. Oxygen saturation in the bone marrow of healthy volunteers [letter]. Blood. 2002;99:394.

41. Cemanec J, Guilak F, Weinberg JB, Piestsky DS, Fermor B. Influence of hypoxia and reoxygenation on cytokine-induced production of proinflammatory mediators in articular cartilage. Arthritis Rheum. 2002;46:968-975.

42. Piellet S, Guyader NL, Hofer T, et al. Hypoxia enhances human B19 erythrovirus gene expression in primary erythroid cells. Virology. 2004;327:1-7.

43. Fu Y, Ishii KK, Munakata Y, Saito T, Kaku M, Sasaki T. Regulation of tumor necrosis factor α promoter by human parvovirus B19 NS1 through activation of AP1 and AP2. J Virol. 2002;76:5359-5365.

Reconstitution of the functional human hematopoietic microenvironment derived from human mesenchymal stem cells in the murine bone marrow compartment

Yukari Muguruma, Takashi Yahata, Hiroko Miyatake, Tadayuki Sato, Tomoko Uno, Jobu Itoh, Shunichi Kato, Mamoru Ito, Tomomitsu Hotta, and Kiyoshi Ando

Hematopoiesis is maintained by specific interactions between both hematopoietic and nonhematopoietic cells. Whereas hematopoietic stem cells (HSCs) have been extensively studied both in vitro and in vivo, little is known about the in vivo characteristics of stem cells of the nonhematopoietic component, known as mesenchymal stem cells (MSCs). Here we have visualized and characterized human MSCs in vivo following intramedullary transplantation of enhanced green fluorescent protein-marked human MSCs (eGFP-MSCs) into the bone marrow (BM) of nonobese diabetic/severe combined immunodeficiency (NOD/SCID) mice. Between 4 to 10 weeks after transplantation, eGFP-MSCs that engrafted in murine BM integrated into the hematopoietic microenvironment (HME) of the host mouse. They differentiated into pericytes, myofibroblasts, BM stromal cells, osteocytes in bone, bone-lining osteoblasts, and endothelial cells, which constituted the functional compo- nents of the BM HME. The presence of human MSCs in murine BM resulted in an increase in functionally and phenotypi- cally primitive human hematopoietic cells. Human MSC-derived cells that reconsti- tuted the HME appeared to contribute to the maintenance of human hematopoi- esis by actively interacting with primitive human hematopoietic cells. (Blood. 2006; 107:1878-1887)

© 2006 by The American Society of Hematology

Introduction

Mesenchymal stem cells (MSCs) present in bone marrow (BM) are thought to give rise to cells that constitute the hematopoietic microenvironment (HME).[1] MSCs have been isolated from BM and various tissues from humans and many other species, expanded in culture, and shown to differentiate into osteocytes, chondrocytes, adipocytes, and myoblasts under defined conditions in vitro.[2] In culture, MSCs produce a number of cytokines and extracellular matrix proteins and express cell adhesion molecules, all of which are involved in the regulation of hematopoiesis.[3,4] They also support the development of hematopoietic colonies in vitro.[4] However, in contrast to hematopoietic stem cells (HSCs) that have been prospectively isolated and extensively studied at the single-cell level both in vitro and in vivo, MSCs have only been defined and isolated by physical and functional properties in vitro. Consequently, little is known about their phenotypic and functional characteristics in vivo.

Systemic administration of MSCs for facilitation of bone marrow transplantation has been proposed based on the in vitro characteristics of MSCs.[5] In recent studies, cotransplantation of human MSCs and HSCs resulted in increased chimerism or accelerated hematopoietic recovery (or both) in animal models and in humans,[6-9] suggesting a role for MSCs in the engraftment and repopulation of HSCs. Although the existence of donor MSCs has been documented in the BM of recipient animals following MSC infusion,[9,10] the methods used to detect engraftment, such as polymerase chain reaction (PCR) or staining of cytospin samples, could not unambiguously distinguish engraftment from cell survival or nonspecific lodgment on the vascular bed. In addition, Awaya et al examined stromal cells of patients who received BM transplants and confirmed that all donor signals were, in fact, derived from macrophages.[11] To our knowledge, there is no physical evidence that transplanted human MSCs have indeed engrafted in the BM of adult animals and directly participated in the enhanced engraftment of HSCs.

To assess the engraftment, spatial distribution, and lineage commitment of MSCs as well as their roles in hematopoiesis in vivo, we transplanted enhanced green fluorescent protein (eGFP)-marked human MSCs into the tibiae of nonobese diabetic/severe combined immunodeficiency (NOD/SCID) mice by intra-bone marrow transplantation (IBMT), a method previously shown to improve the engraftment of both hematopoietic and nonhemato- poietic cells in mice.[12-14] We used a dual-color genetic marking strategy[15] along with immunofluorescent staining to distinguish and investigate transplanted cells in situ. We show that trans- planted human MSCs integrated into the functional components of the HME and that these MSC-derived cells appeared to be actively involved in the maintenance of human hematopoiesis in murine BM.

Materials and methods

Isolation of human cord blood CD34+ cells

Human umbilical cord blood (CB) samples were obtained from full-term deliveries with informed consent of the mother and used in accordance with the institutional guidelines approved by the Tokai University Committee on Clinical Investigation. CD34+ cells were selected using the CD34 Progenitor Cell Isolation Kit (Miltenyi Biotec, Sunnyvale, CA) according to the manufacturer's instructions as described previously.[12] The purity of selected cord blood CD34+ (CBCD34) cells was always greater than 95%, and they were cryopreserved in liquid nitrogen until use. In some experiments, CBCD34 cells were further fractionated into CD34+CD38+ and CD34+CD38- populations at the day of transplantation.

Human MSCs

Human MSCs were purchased from Cambrex BioScience Walkersville (Walkersville, MD) and cultured according to the directions supplied by the company. The ability to differentiate into adipocytes, chondrocytes, and osteoblasts was confirmed in vitro before they were used for the experiments.[2]

Antibodies

The following antibodies were used for tissue immunostaining: anti-CD15 (80H5, 1:75; Coulter/Immunotech, Marseille, France), anti-CD31 (1:100; TECNE, Minneapolis, MN), anti-CD34 (My10, 1:20; BD Biosciences, San Jose, CA), anti-CD45 (2D1, 1:75; BD Biosciences), anti–glycophorin A (JC159, 1:400; Dako, Glostrup, Denmark), anti–N-cadherin (1:20; IBL, Gunma, Japan), antiosteocalcin (1:25; Biogenesis, Poole, United Kingdom), anti–smooth muscle (SM) actin (1A4, 1:800; Sigma-Aldrich, St Louis, MO), anti–alkaline phosphatase (B4-78, 1:30; Developmental Studies Hybridoma Bank, University of Iowa, Iowa City, IA), antivimentin (1:400; Progen Biotechnik, Heidelberg, Germany), anti-GFP (1:500; MBL, Nagoya, Japan), antiosteopontin (10A16, 1:100; IBL), and anti–SDF-1 (1:200, Santa Cruz Biotechnology, Santa Cruz, CA). The following monoclonal antibodies (mAbs) were used for flow cytometry: fluorescein isothiocyanate–conjugated anti-CD19 (SJ25C1; BD Biosciences), phycoerythrin-conjugated anti-CD33 (WM53) and anti-CD34 (581), and allophycocyanin-conjugated anti-CD45 (J.33; all from Coulter/Immunotech).

Experimental animals, lentiviral gene transduction, and cell transplantation

Eight- to 10-week old male NOD/Shi-scid (NOD/SCID) mice were purchased from Clea Japan (Tokyo, Japan) and housed in sterile microisolator cages in the animal facility of Tokai University School of Medicine. Mice were given autoclaved food and water. Twenty-four hours before transplantation, mice were irradiated with 300 cGy from an x-ray irradiator (HW-300, Hitex, Osaka, Japan) and thereafter fed acidified water. All procedures were approved by the Animal Care Committee of Tokai University. Prior to transplantation into mice, MSCs and CBCD34 were genetically marked with eGFP or its yellow variant enhanced yellow fluorescent protein (eYFP). Transduction of CBCD34 and MSCs was carried out as described previously.[15,16] For in situ examination of transplanted cells, 1 × 10⁶ eGFP-marked MSCs and 2 × 10⁵ eYFP-marked CBCD34, 2 to 4 × 10⁵ CD34+CD38+ cells, or 1.5 to 4 × 10⁴ CD34+CD38- cells were suspended in 10 μL PBS and transplanted directly into the right tibia of NOD/SCID mice using a Hamilton syringe equipped with a 31-gauge needle.[12] In some experiments, gene-marked MSCs or CBCD34 cells were separately transplanted by IBMT or by the intravenous route.

Analysis of human cell homing

Staining of CBCD34 cells with PKH26 dye (Sigma-Aldrich) and analysis of cells that homed into BM were conducted as described previously.[12] Each mouse received 1 × 10⁶ MSCs into the right tibia and 10 μL PBS into the left tibia by IBMT, followed by administration of 1 × 10⁶ PKH26-labeled CBCD34 cells into the retro-orbital plexus. Twenty hours after transplantation, mice were humanely killed, and BM cells were collected separately from the tibiae that had been injected with MSC and the PBS.

Analysis of human cell engraftment

A total of 1 × 10⁶ MSCs was injected into the right tibiae of irradiated NOD/SCID mice, and then 5 × 10⁴ CBCD34 cells were injected into the retro-orbital plexus of the mice. Control groups received the same amount of PBS in the right tibia. At 6 weeks after transplantation, mice were humanely killed, and BM cells were collected separately from each tibia. Aliquots of cells were used to examine the percentages of CD45-, CD19-, CD33-, and CD34-expressing cells in the respective tibia. Two-color flow cytometric analysis was conducted using FACSCalibur. Quadrants were set to include at least 97% of the isotype-negative cells. The proportion of each lineage was calculated from 20 000 events acquired using CellQuest software (Becton Dickinson, San Jose, CA). Remaining cells were saved for the clonogenic cell assay and secondary transplantation.

Clonogenic cell assay

Human hematopoietic cells were isolated from BM cells of mice given transplants using CD45 MicroBeads (Miltenyi Biotec) according to the manufacturer's protocol. The purity of selected cells was 36% to 96% (mean, 73%). CD45-enriched populations containing 10 000 CD45+ cells were plated in MethoCult GFH4434V (StemCell Technologies, Vancouver, BC, Canada). The number and morphology of colonies formed during the 14-day culture period were determined under inverted microscope. Morphologic designation of colony type by light microscopy was confirmed by Wright-Giemsa staining of cytospin preparations. The specificity of the assay was confirmed by PCR on individual colonies using primers specific for the human chromosome 17-α satellite sequence[12] and the expression of CD45 by flow cytometric analysis.

Secondary transplantation

BM cells obtained separately from each tibia of primary mice were intravenously transplanted into irradiated secondary recipient mice. Because the number of cells recovered from one tibia was small (2.4-3.5 × 10⁶/tibia), we used NOD/SCID IL-2Rγ^null mice, which have been shown to be a better recipient of human cells than NOD/SCID mice,[17,18] as secondary recipients. Six weeks after transplantation, BM cells were obtained from tibiae and femurs of each secondary recipient, and the presence of human cells was analyzed by flow cytometry.

Tissue processing and immunofluorescent staining

Anesthetized mice were perfused with 4% paraformaldehyde in PBS. The tibiae were excised, decalcified, infiltrated with sucrose, embedded in OCT compound (Sakura, Tokyo, Japan), and frozen in liquid nitrogen. Frozen sections of decalcified bone were obtained using a cryostat microtome (CM3050, Leica, Germany) and stored at −80°C until staining. Immunofluorescent staining and enzyme immunohistochemistry were performed as described previously.[16] For immunofluorescent analysis, slides were examined and images were captured using an LSM510 META confocal microscope and a 63 ×/1.2 numeric aperture (NA) c-Apochromat objective lens (Carl Zeiss, Jena, Germany). Images were transferred to Adobe Photoshop 7.0 (Adobe Systems, San Jose, CA).

Quantitative microscopic examination

Spatial distribution of human hematopoietic cells. The location of cells was designated as either endosteal (within 12 cells of the endosteum) or central (>12 cells of the endosteum) as described previously.[19] To accurately assess the proportion of endosteal area, the diameter of the diaphyseal shaft was evaluated by counting the number of cells from one side of the endosteum to the other along the line perpendicular to the longitudinal axis of the bone. CD34-, CD15-, and glycophorin A–reactive

human hematopoietic cells present in the diaphyseal shaft were counted under light microscopy with assistance of a Zeiss KS400.

Interaction between human MSCs and human HSCs. Entire fields of longitudinal sections cut through the center of bones were examined for cell counting. All eGFP-expressing cells and immunophenotyped human hematopoietic cells present in BM were counted under fluorescent microscopy. When cells were in physical contact, they were categorized as interacting.

Statistical analysis

All values are presented as the mean plus or minus standard deviation (SD). The 2-sided P value was determined, testing the null hypothesis that the 2 population medians are equal. P below .05 was considered significant.

Results

Spatial distribution of human hematopoietic cells in the murine BM compartment

The potential of human HSCs in vivo can be assessed by using the SCID-repopulating cell (SRC) assay based on the ability to reconstitute hematopoiesis in the host following transplantation into NOD/SCID mice.[20] However, analysis of SRCs by flow cytometry does not allow identification of individual SRCs in situ. Consequently, the behavior of transplanted SRCs during repopulation has not been elucidated. To address this issue, we prepared mice that were highly chimeric with human hematopoietic cells by directly injecting CBCD34 cells into the tibia[12] and investigated the spatial organization of individual engrafted cells in murine BM at 10 weeks after transplantation. Close examination of the bone specimens revealed that cells stained positive for human CD34, a marker of human HSCs and progenitor cells, were specifically localized to an area near the endosteum of the bone (the endosteal region) (Figure 1A). In contrast, cells positively stained for human CD15, a marker of committed myelocytes, or glycophorin A (GlyA), a marker of the erythrocyte lineage, were distributed distant to the endosteum (Figure 1B-C). These results reflect previous morphologic studies of BM that found that hematopoietic stem and progenitor cells are concentrated in the endosteal region rather than the central marrow area, which mostly is composed of mature cells.[19,21,22] To quantitatively confirm these observations, the numbers of CD34$^+$, CD15$^+$, and GlyA$^+$ cells present in the endosteal region or in the central BM cavity of the diaphyseal shaft were counted. Consistent with the microscopic observations, a surprisingly higher proportion of CD34$^+$ cells was located in the endosteal region compared to the lineage-committed cells (Table 1). Because the endosteal region consisted of only 21.4% ± 3.8% of the BM cavity examined for this assay, there were approximately 10-fold more CD34$^+$ cells in the endosteal area. By visualizing the fate of transplanted SRCs in situ and confirming their physiologic organization in BM, these results validate the SRC assay for human cell analysis. Hence, we used this xenogeneic transplantation system for the phenotypic and functional characterization of human MSCs in vivo.

Visualization of human MSCs and human CBCD34 engraftment in the murine BM compartment

The route of administration is an important factor for effective delivery of transplanted cells into the target tissue. We compared the degree of cell engraftment in BM at 4 and 10 weeks after IBMT or intravenous transplantation of eYFP-marked CBCD34 cells
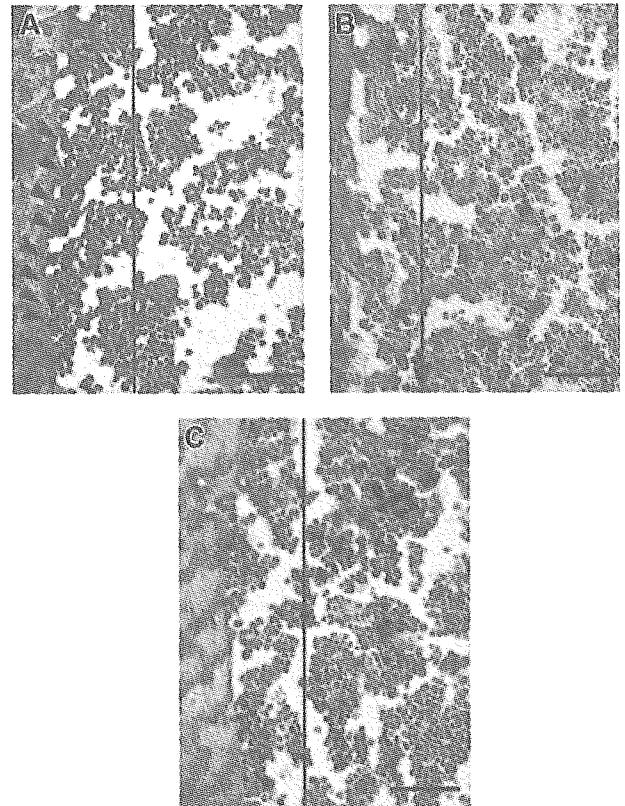
Figure 1. Spatial distribution of human hematopoietic cells in the murine BM compartment. Representative pictures of bone specimens from NOD/SCID mice at 10 weeks after IBMT of 2 × 10⁵ CBCD34 cells are shown. Slides were stained with either anti-CD34, anti-CD15, or anti–glycophorin A antibody, and cells expressing the respective antigens were distinguished by brown reactive products of DAB on immunohistochemistry. CD34$^+$ cells are localized to the endosteal region (A; black arrowheads), whereas CD15$^+$ (B) and GlyA$^+$ cells (C) are distributed away from the endosteum. Vertical lines demarcate 12 cells of the endosteum. Bars represent 100 μm. Images were obtained using an Olympus AX80 microscope and a 20 ×/0.7 NA UPlanApo objective lens. Images were captured using a DP50 digital camera fitted with Viewfinder Lite (all from Olympus, Tokyo, Japan).

(eYFP-CBCD34; Figure 2A) or eGFP-marked MSCs (eGFP-MSCs; Figure 2B). When excess numbers of eYFP-CBCD34 cells (2 × 10⁵) were transplanted intravenously or by IBMT, similar amounts of eYFP$^+$ human hematopoietic cells (eYFP-cells) that expressed human CD45, a pan-leukocyte marker, were observed in BM at both time points examined (Figure 2C-D and data not shown). In marked contrast to the sufficient engraftment of human hematopoietic cells, intravenous administration of 1 × 10⁶ eGFP-MSCs resulted in virtually no visible MSCs in BM at either 4 (Figure 2F) or 10 weeks after transplantation. At 10 weeks after transplantation, analysis of 250 bone sections prepared from 5 mice yielded a total of only 10 eGFP-MSCs in BM. However, when the same number of MSCs was administered by IBMT, eGFP-MSCs were clearly identified in BM at the both time points. At 4 weeks after transplantation, eGFP-MSCs were broadly distributed in BM (Figure 2G-H). At 10 weeks after transplantation, eGFP-MSCs were detected in all sections examined (> 1000 sections), although the number of eGFP-MSCs per section varied considerably (range, 1-57; median, 13; mean, 14.8; from 91 sections) depending on the plane of sectioning. Interestingly, unlike eYFP-cells, which migrated into the contralateral tibia,[12] no eGFP-MSCs were detected in the BM of the tibia that had not received injections (data not shown), suggesting no or minimal migration of transplanted MSCs in this system.

Table 1. Spatial distribution of human hematopoietic cells in the murine BM compartment at 10 weeks after IBMT of CBCD34

	Total no. cells counted	Total no. cells in the endosteal region	Cells in the endosteal region/slide, %
CD34	1469	1086	71.4 ± 12.5*
CD15	2940	451	14.9 ± 6.2
GlyA	1514	171	10.7 ± 2.2

Fourteen slides from at least 8 different mice were examined to count each cell type. Slides containing 115 ± 19 cells in the diaphyseal shaft were chosen for this analysis. Because the endosteal region was arbitrarily decided within 12 cells of both endosteum, the endosteal area comprised approximately 21.4% ± 3.8% of the BM cavity in this study. The proportion of cells located in the endosteal area was calculated for each slide and expressed as the means ± SD.

*$P < .001$ relative to the CD15 and GlyA groups.

Integration of human MSCs into the murine microenvironment

Having confirmed the effectiveness of delivering MSCs into BM, IBMT was used for all subsequent experiments. The phenotypes of transplanted MSCs and their progeny at 10 weeks after transplantation were investigated in detail. In contrast to the bone specimens prepared at 4 weeks after transplantation, in which eGFP-MSCs were located throughout the marrow cavity (Figure 2G-H), eGFP-MSCs at 10 weeks after transplantation were preferentially localized to the endosteal region (73.8% ± 18.4%, n = 251 eGFP-MSCs), frequently within 5 cells from the surface of the bone. When human MSC-derived eGFP-expressing cells (eGFP-cells) were found away from the endosteum, they were often associated with the vasculature (Figure 3A,D). Those vasculature-associated eGFP-cells expressed α-SM actin (Figure 3B-C,E-F), the expression of which has been documented in pericytes, SM cells of the vascular wall as well as myofibroblasts in BM.[23,24] A total of 59.9% ± 21.6% of eGFP-cells (n =251) found in BM were positive for α-SM actin.

Two other types of eGFP-cells that were negative for α-SM actin were also present in BM: flattened cells located in the hematopoietic cords but not specifically associated with the vasculature (Figure 3G) and cells characterized by long cytoplasmic extensions, so-called reticular cells (Figure 3H) that are considered to be the predominant cells of the HME.[25,26] BM was often interspersed with a fine network of cell processes that expressed alkaline phosphatase (ALP; Figure 3I), an enzyme that distinguishes reticular cells from the stromal component of acid phosphatase– or nonspecific esterase–expressing macrophages.[11,25] A total of 28.2% ± 11.2% of eGFP-cells (n = 242) in BM were ALP+.

In addition, eGFP-cells were found within or on the surface of the bone (Figure 3J-O). Cells in the bone stained positive for osteocalcin, a specific marker of mature osteoblasts and osteocytes (Figure 3K-L), indicating an active participation in skeletal remodeling.[27,28] Interestingly, eGFP-cells on the bone surface resembled spindle-shaped osteoblasts (Figure 3M; see also Figure 7), a key component of the stem cell niche in murine hematopoiesis.[29-32] These cells expressed osteopontin (data not shown) and N-cadherin (Figure 3M-O), both of which are involved in regulating murine HSCs.[29,33,34] In a small number of mice examined (4 of 39), eGFP-cells associated with the vasculature stained positive for CD31 (Figure 3P-R) and CD34 (Figure 3S-U), markers of endothelial cells. MSCs expanded ex vivo prior to transplantation did not react with any of these markers either by the immunohistochemical or flow cytometric method, but they did stain positive for vimentin, a marker of fibroblasts (data not shown). These results indicate that

within 10 weeks after transplantation, human MSCs differentiated into pericytes, myofibroblasts, reticular cells, osteocytes in bone, bone-lining osteoblasts, and endothelial cells, which constitute the 3-dimensional structure of hematopoietic parenchyma and provide the milieu of hematopoiesis.[26] Therefore, we designated these cells as human MSC-derived hematopoietic microenvironment reconstituting cells (HMRCs).

Engraftment of human hematopoietic cells

During analysis of the engraftment and differentiation of transplanted MSCs, we frequently observed physical contact between HMRCs and hematopoietic eYFP-cells (Figure 3A-I). In particular, eYFP-cells were intimately associated with ALP+ eGFP-reticular cells, where eYFP-cells were almost surrounded by the thin delicate cytoplasm of the eGFP-reticular cells (Figure 3H-I). To address whether the presence of HMRCs in the murine HME contributes to the development of human hematopoietic cells, we analyzed the engraftment and differentiation of CBCD34 cells after transplantation with or without human MSCs. MSCs were injected into the right tibiae of irradiated NOD/SCID mice by IBMT, and then CBCD34 cells were administered intravenously into each mouse. Consistent with our histologic findings, more human CD45+ cells were found in the tibiae into which MSCs had been injected than the tibiae that had not received injections. In addition, the presence of MSCs increased the percentage of CD34+ cells
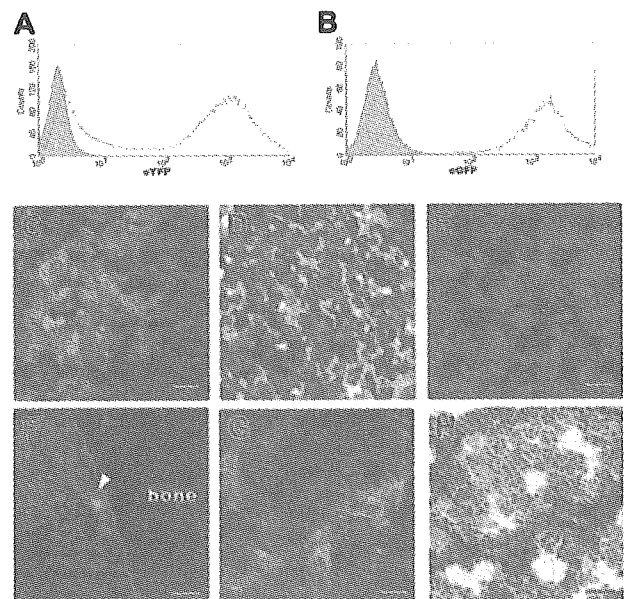
Figure 2. In situ visualization of human MSCs and hematopoietic cells in the murine BM compartment at 4 weeks after IBMT or intravenous transplantation. Transduction efficiencies of eYFP into CBCD34 cells and eGFP into MSCs, determined by flow cytometric analysis at the day of transplantation, were approximately 65% (A) and 99% (B), respectively. The shaded histograms indicate nontransduced cells. (C-E) The presence of human hematopoietic cells was determined by eYFP fluorescence and immunofluorescence staining with an anti-human CD45 antibody followed by Alexa-fluor 594 goat anti-mouse immunoglobulin secondary antibody. Cell nuclei were visualized by staining with TOTO3. Similar amounts of eYFP-cells expressing human CD45 (red) are present in BM after intravenous transplantation (C) or IBMT (D). (E) No eYFP- or CD45-reactive cells are present in the BM of noninjected mouse. (F) eGFP-MSCs are rarely seen in BM after intravenous transplantation (white arrowhead). After IBMT, eGFP-MSCs are easily identified in the BM cavity by eGFP fluorescence (G) and immunohistochemistry (H). (G-H) The same section was stained with an anti-GFP antibody after examining for eGFP fluorescence. All bars represent 10 μm. Images in panels C-G were obtained using an LSM510 META confocal microscope; image in panel H was obtained using an Olympus AX80 microscope and a 20 ×/0.7 NA UPlanApo objective lens.
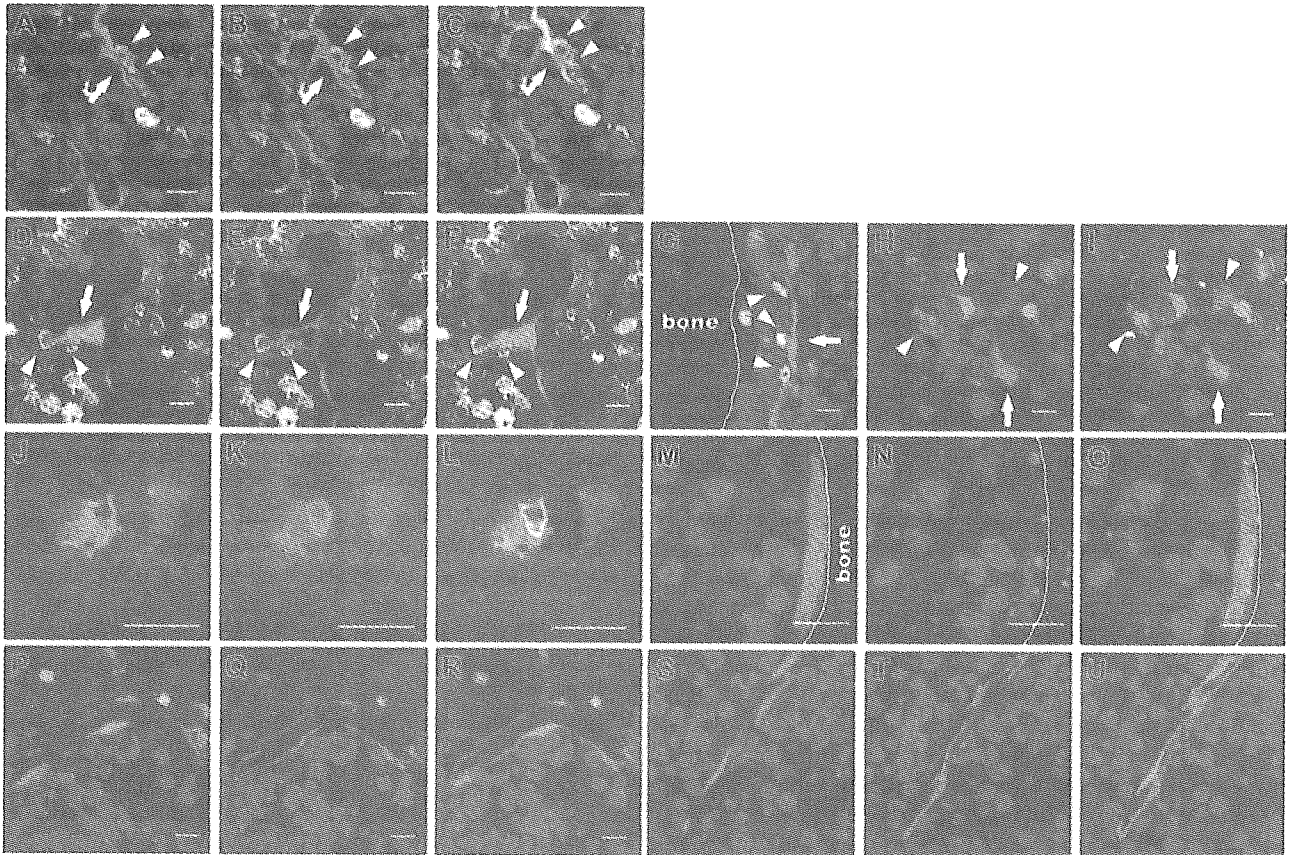
Figure 3. Site-specific differentiation of human eGFP-MSCs in the murine BM compartment. The engraftment and differentiation of transplanted eGFP-MSCs were determined by eGFP fluorescence and immunofluorescence staining for lineage-specific antigens. eGFP-cells were located on the abluminal side of endothelial cells (A) or lined the sinus wall (D). Those vasculature-associated eGFP-cells express α-SM actin (red in panels B and E, and merged in panels C and F). (A-F) eYFP-cells reside next to eGFP-cells. (G) An elongated cell in the endosteal hematopoietic cord interacts with eYFP-cells. eGFP-reticular cells (H) with ALP⁺ (red) cytoplasmic extensions (I), which haphazardly radiate into the hematopoietic parenchyma, interact with eYFP-cells. An eGFP-cell in the bone exhibits the morphology of authentic osteocytes with filopodial processes surrounded by bone matrix and extending into the canaliculi (J), and expresses osteocalcin (red, K-L). A bone-lining eGFP-cell (M) expresses N-cadherin (red, N-O). N-cadherin is localized to the cell surface. Vasculature-associated eGFP-cells (P,S) express CD31 (red, Q-R) and CD34 (red, T-U). Interactions between eGFP-cells (arrows) and eYFP-cells (arrowheads in A-I) are seen in the specimens from mice in which eGFP-MSCs and eYFP-CBCD34 were cotransplanted. All bars represent 10 μm.

without affecting the proportion of CD19⁺ B lymphocytes or CD33⁺ myeloid cells (Figure 4A). There were 2-fold more human CD45⁺ cells in the tibiae into which MSCs had been injected compared with the tibiae that had not received injections (25.7% ± 17.6% versus 12.8% ± 11.1%, P = .002, Figure 4B), and the absolute number of CD34⁺ cells present in the tibiae into which MSCs had been injected was 3-fold higher than that in the tibiae that had not received injections (99 296 ± 68 189 versus 31 525 ± 25 224; P = .007, Figure 4C). Control experiments, in which the same volume of PBS was injected into the right tibia, were conducted to exclude the possibility that this effect was due to injury from the injection. There were no significant differences in either the percentage of CD45⁺ cells or the number of CD34⁺ cells between the tibiae into which PBS had been injected and the contralateral tibiae (Figure 4B-C). We then examined the colony-forming ability of BM cells recovered from the mice that had received injections of MSCs and control mice given PBS. The cumulative numbers of colony-forming cells (CFCs) recovered from both tibiae of experimental animals were 2663 for the group that had received injections of MSCs and 1578 for the control group (n = 3 for each group). The proportion of colony types formed from BM cells obtained from both groups was similar (data not shown). Because the numbers of CFCs recovered from each experimental animal varied considerably, we compared the proportion of CFCs present in the tibiae into which MSCs had been

injected with the tibiae that had not received injections over the total number of CFCs in each animal. In mice given MSCs, the tibiae into which MSCs had been injected contained the majority of CFCs (89.4% ± 6.7% versus 10.6% ± 6.7%, P = .007), whereas CFCs were evenly distributed in the right and left tibiae (53.3% ± 18.1% and 46.7% ± 18.1%, respectively) in control mice (Figure 4D). These results confirmed that the presence of human MSCs positively affected the engraftment of human HSCs.

To assess if there were any functional differences between human cells engrafted in the tibiae into which MSCs had been injected and tibiae that had not received injections, we transplanted BM cells obtained from each tibia of primary mice to separate secondary hosts. Two of 3 secondary host pairs showed human cell engraftment. A pair of recipients, which received cells from the primary host with minimal engraftment (CD45% content; 1.44% for tibiae into which MSCs had been injected and 0.52% for tibiae that had not received injections), failed to show engraftment. As expected, secondary hosts that received BM cells of the tibiae into which MSCs had been injected demonstrated a markedly higher level of engraftment than the hosts that received cells of tibiae that had not received injections (Figure 4E). Taken together, the presence of HMRCs in murine BM augmented not only the proportion of human cells but also the function of human cells engrafted in mouse BM.

Figure 4. Effect of human MSCs on the engraftment of human hematopoietic cells. (A) BM cells obtained from the MSC-injected or noninjected tibia from the same mouse were examined by flow cytometry at 6 weeks after transplantation. Representative flow cytometric profiles are shown. The relative frequencies of each population are shown at the corner of the respective quadrants. The numbers in parentheses indicate the proportion of CD45⁺ cells positive for each marker. (B) Percentages of human CD45⁺ cells in the right (injected) and the left (noninjected) tibia of the MSC-injected (MSC) and control mice (CT). (C) Absolute numbers of CD34⁺ cells in the right and the left tibia of the MSC-injected and control mice. Each white circle represents one mouse. Values obtained from the same mouse are connected with lines. (D) Distribution of clonogenic progenitors into the right and the left tibia of the MSC-injected and control mice. The proportions of clonogenic cells present in the respective tibia over the total number of clonogenic cells recovered from both tibiae of each mouse are shown (n = 3). *$P < .05$ and **$P < .01$ relative to the noninjected (left) tibia. (E) Secondary transplantation. BM cells obtained separately from the MSC-injected or noninjected tibia from the same mouse were transplanted into separate secondary hosts. Human cell engraftment was analyzed by CD45 expression at 6 weeks after transplantation. Results of 2 pairs of secondary host are shown. Numbers in parentheses above each flow cytometric profile show the percentage of CD45 cells in the BM cells of primary host. The relative frequencies of CD45 cells in secondary hosts are shown in each profile.
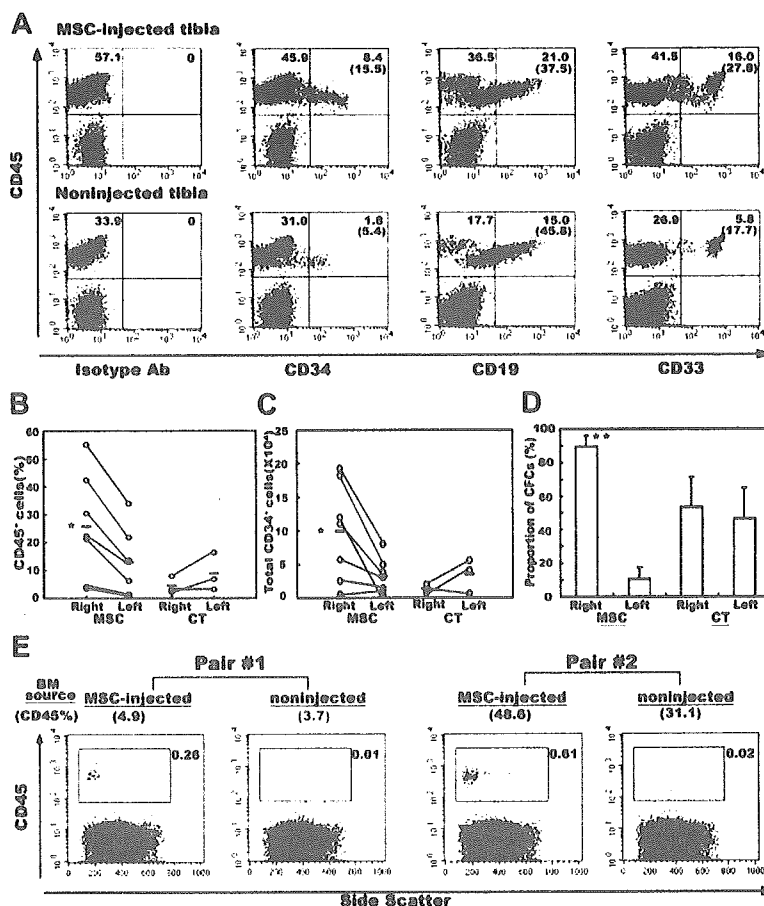
## Interaction between human MSC-derived cells and human hematopoietic cells

Having shown the effect of MSCs on human hematopoietic cell engraftment, we examined the underlying basis of increased engraftment in phenotypically and functionally primitive cells. First, we asked whether MSCs play a role in the migration and homing of HSCs to BM, critical steps in the engraftment and initiation of hematopoiesis after transplantation. Prior to intravenous administration of CBCD34, each mouse was given injections of MSCs into the right tibia and PBS into the left tibia. The percentages of CBCD34 cells homed to the tibiae into which MSCs and PBS had been injected were not different (0.05% ± 0.02% and 0.04% ± 0.01%, respectively; n = 3). Thus, MSCs did not seem to function in the initial homing of CBCD34 cells.

We then asked whether MSCs participate in the repopulation process of human hematopoietic cells in the murine HME. At 10 weeks after transplantation, human MSC-derived HMRCs and CBCD34-derived hematopoietic cells frequently interacted (Figure 3), suggesting the role of HMRCs in the maintenance of human hematopoiesis. When those hematopoietic cells were immunophenotyped, CD34⁺ cells were often in contact or within close proximity to HMRCs (Figure 5Ai), contrasting to lineage-committed CD15⁺ and GlyA⁺ cells that were usually found away from HMRCs (Figure 5Aii-iii). Interestingly, one HMRC interacted with 7 CD34⁺ cells (Figure 5Aiv). These results suggest that HMRCs interact specifically with primitive human hematopoietic cells; therefore, we quantitated HMRCs that were in physical contact with CD34⁺, CD15⁺, or GlyA⁺ cells (Table 2; Figure 5B). Whereas approximately half of all HMRCs in BM were in contact

with CD34⁺ cells, less than 4% of HMRCs were in contact with the lineage-committed cells (Figure 5Bi). Furthermore, the vast majority of HMRCs located in the endosteal region interacted with CD34⁺ cells (Figure 5Bii). We then examined the human hematopoietic cells that were in contact with HMRCs. A significantly higher proportion of CD34⁺ cells interacted with HMRCs compared to the lineage-committed cells (Figure 5Biii). The proportion of CD34⁺ cells interacting with HMRCs in the endosteal region was 2-fold higher than that of CD34⁺ cells in the central marrow (Figure 5Biv). The result suggests that CD34⁺ cells in the endosteal region and the central marrow represent different populations of CD34⁺ cells.

Because the heterogeneity among CD34⁺ stem/progenitor cells is known,[35-39] we further examined the interaction between CD34⁺ cells and HMRCs by transplanting SRC-enriched CD34⁺CD38⁻ cells or more mature CD34⁺CD38⁺ progenitor cells together with MSCs (Figure 6). At 1 week after transplantation, there were no differences in the proportions of CD34⁺ cells localized to the endosteal region (27.4% ± 7.8% for the CD34⁺CD38⁻ group and 26.5% ± 12.1% for the CD34⁺CD38⁺ group) or CD34⁺ cells interacting with HMRCs (8.1% ± 10.2% and 8.2% ± 9.7%, respectively) between the 2 experimental groups. At 3 weeks after transplantation, the proportion of CD34⁺ cells in the endosteal area was 2-fold higher in the group that had received transplants of SRC-enriched CD34⁺CD38⁻ cells (63.3% ± 7.9% versus 33.1% ± 8.3%; $P < .001$). To our interest, a significantly higher proportion of CD34⁺ cells were in contact with HMRCs in the group that had received transplants of CD34⁺CD38⁻ cells (9.4% ± 4.8% versus 4.4% ± 4.0%; $P < .05$). In the group that

A

B
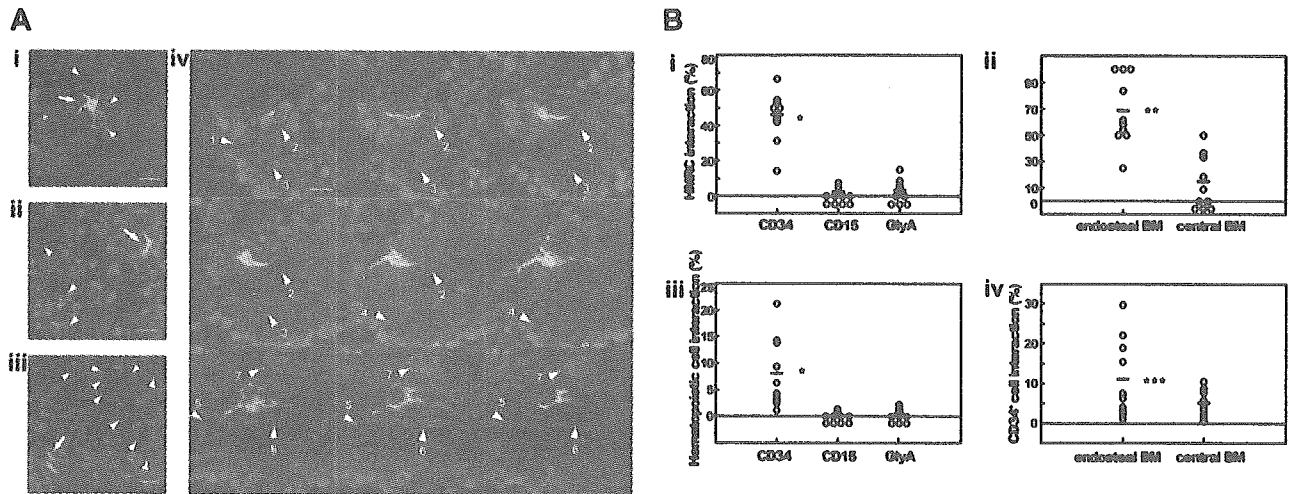
Figure 5. Interaction between HMRCs and CD34+, CD15+, or GlyA+ cells. (A) Bone slides were stained with either anti-CD34, anti-CD15, or anti–glycophorin A antibody followed by Alexa-fluor 594 goat anti–mouse immunoglobulin secondary antibody, and examined under fluorescent microscope. (Ai) CD34+ cells are in physical contact with the cell body and cytoplasmic extensions of a HMRC. CD15+ (Aii) or GlyA+ cells (Aiii) are not found close to HMRCs. HMRCs and immunophenotyped cells are indicated by arrows and arrowheads, respectively. (Aiv) One HMRC in the hematopoietic parenchyma interacts with 7 CD34+ cells (numbered arrowheads). Numerical letters at the left corner of each panel indicate the position of z-axis in the analytical planes. All bars represent 10 μm. (B) Quantification of the interaction between HMRCs and CD34+, CD15+, or GlyA+ cells. (Bi) Frequencies of HMRCs interacting with CD34+· CD15+, or GlyA+ cells. (Bii) The vast majority of HMRCs located in the endosteal region interact with CD34+ cells. (Biii) Frequencies of CD34+, CD15+, or GlyA+ cells interacting with HMRCs. (Biv) In the endosteal region, 2-fold more CD34+ cells interact with HMRCs than in the central marrow. Each white circle represents a value obtained by counting. *P < .005 relative to the CD15 and GlyA groups; **P < .005 and ***P < .05 relative to the central group.

had received CD34+CD38+ transplants, CD34+ cells interacting with HMRCs became progressively rarer (8.2% ± 9.7% at 1 week and 4.4% ± 4.0% at 3 weeks) and were rarely observed at 6 weeks after transplantation (1.1% ± 1.0%). At both time points examined, the group that had received CD34+CD38− transplants contained higher proportions of CD34+ cells interacting with bone-lining osteoblasts (9.3% ± 10.9% versus 2.7% ± 5.5% at 1 week and 32.4% ± 16.8% versus 17.4% ± 9.9% at 3 weeks). This tendency of CD34+CD38− cells, the preferential localization of CD34+ cells in the endosteal area and their interaction with bone-lining osteoblasts, may reflect their high repopulation potential. In another words, SRC-enriched CD34+CD38− cells localize to the endosteal area and interact with bone-lining osteoblasts as well as HMRCs, and progressively become distant to the endosteal area as they differentiate into progenitor cells and finally to mature cells. These results confirmed our earlier observation that HMRCs interacted with the primitive population of CD34+ cells, which resulted in the enhanced engraftment of human hematopoietic cells.
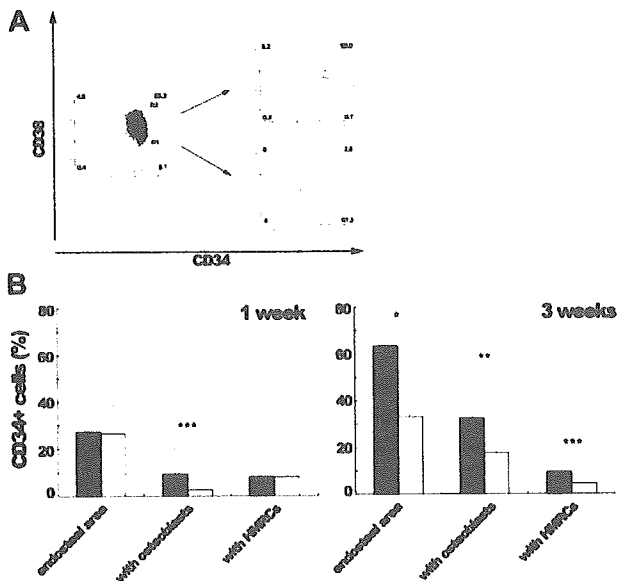
Molecular interaction of HMRCs and CD34+ cells

To determine how HMRCs participated in human hematopoietic cell repopulation in mice, we investigated the molecular interaction of HMRCs and CD34+ cells. We found that CD34+ cells adhered to HMRCs on the bone surface and appeared to proliferate along the endosteal surface, suggesting the existence of specific local signals between CD34+ cells and bone-lining HMRCs (Figure 7A). Double staining for N-cadherin and CD34 demonstrated that bone-lining HMRCs associated with CD34+ cells through the colocalization of N-cadherin (Figure 7B-E). In addition, an HMRC in the endosteal hematopoietic parenchyma expressed stromal cell-derived factor 1 (SDF-1) and interacted with a few eYFP-human hematopoietic cells (Figure 7F-H), although SDF-1 was not detected in ex vivo expanded MSCs by immunofluorescence analysis (data not shown). In BM, SDF-1 is constitutively expressed by osteoblasts, endothelial cells, and BM stromal cells.[40] In addition to its well-established role in homing and retention of HSCs in BM,[41] SDF-1 has been implicated

Table 2. Interactions between HMRCs and human hematopoietic cells at 10 weeks after IBMT of eGFP-MSCs plus CBCD34

	HMRC interaction with hematopoietic cells			Hematopoietic cell interaction with HMRC		
		HMRCs interacting			Hematopoietic cells interacting	
	No. cells counted	Total no.	Frequency, %	No. cells counted	Total no.	Frequency, %
CD34						
Total	150	66	45.9 ± 13.5*	1609	76	8.0 ± 6.2*
Endosteal	81	49	68.0 ± 24.8†	1012	59	11.0 ± 9.4‡
Central	59	17	14.6 ± 17.9	597	17	5.0 ± 3.1
CD15	100	3	1.2 ± 2.4	2603	3	0.14 ± 0.28
GlyA	154	5	3.2 ± 4.5	1624	5	0.36 ± 0.49

BM sections stained with either anti-CD34, anti-CD15, or anti–glycophorin A (GlyA) antibody were examined under fluorescent microscope (10 slides from at least 5 different mice for each cell type). The total numbers of HMRCs and immunophenotyped hematopoietic cells present in the sections were counted, and individual cells were examined for physical contact between HMRCs and hematopoietic cells. Proportions of interacting cells/slide were calculated for each cell type and expressed as the means ± SD. Interactions in CD34+ cell group were further categorized into the endosteal and the central BM groups based on the histoanatomic location of cells.
*P < .005 relative to the CD15 and GlyA groups.
†P < .005 relative to the central group.
‡P < .05 relative to the central group.

Figure 6. In vivo localization of CD34+ cells and their interaction with HMRCs after IBMT of CD34+CD38− or CD34+CD38+ populations together with human MSCs. (A) Sorting profiles of CD34+CD38+ and CD34+CD38− populations. The relative frequencies of each population are shown in the corner of the respective quadrants. (B) At 1 or 3 weeks after IBMT, bone sections were stained with an anti-CD34 antibody and examined for counting. Eighteen slides from 3 mice for each group were counted to obtain the proportion of CD34+ cells localized to the endosteum (endosteal area) at the both time points. CD34+ cells in the endosteal area were further categorized into cells attaching to bone-lining osteoblasts (with osteoblasts) and cells interacting with HMRCs (with HMRCs). The proportions of CD34+ cells in each category are shown. At 1 week after IBMT, the proportions of CD34+ cells both in the endosteal area and in contact with HMRCs were not different between the 2 groups. At 3 weeks after IBMT, the SRC-enriched CD34+CD38−-transplanted group had the higher proportions of CD34+ cells in the endosteal area as well as those interacting with HMRCs. At the both time points examined, the proportion of CD34+ cells interacted with osteoblasts was higher in the SRC-enriched CD34+CD38−-transplanted group. Bars represent the CD34+CD38−-transplanted group (■) and the CD34+CD38+-transplanted group (□). *$P < .001$, **$P < .005$, and ***$P < .05$ relative to the CD34+CD38+ group.

in regulating the status of primitive HSCs both in vitro and in vivo.[42-44] Therefore, HMRCs may contribute to the maintenance of primitive human HSCs through N-cadherin–mediated interactions and the production of SDF-1.

Discussion

Our study demonstrated that intramedullary transplanted human MSCs reconstituted the HME and provided direct evidence for a role of transplanted human MSCs in the enhancement of human hematopoietic cell repopulation in mice. The initial histologic analysis unveiled the integration of human hematopoietic cells into the specially and functionally compartmentalized HME of NOD/SCID mice. Based on this finding, we established a model system that enables the identification of the phenotype and function of human MSCs in vivo by directly injecting genetically marked human MSCs into the BM of NOD/SCID mice. Analogous to human HSCs, human MSCs persisted long-term in murine BM to at least 10 weeks after transplantation and were able to differentiate into the key components of the HME in the host. The presence of human MSCs in murine BM correlated with the increase in human hematopoietic cells that were phenotypically and functionally primitive. Engrafted human MSCs appeared to be involved in the maintenance of human hematopoiesis via secreted factors as well as by physically interacting with primitive hematopoietic cells.

The stem cell niche is a key determinant of stem cell development.[45,46] We are beginning to understand the murine HSC niche and the molecular mechanisms that govern the fate of murine HSCs,[47] but there exists a paucity of data on the cellular and molecular microenvironmental regulation of human hematopoiesis in vivo due largely to a lack of good experimental tools. Although the identification of SRCs has facilitated detailed characterization of human HSCs in vivo,[20,48] the key niches that function in human cell repopulation have not been identified. Our study has demonstrated for the first time that CD34-expressing stem/progenitor cells localize to the endosteal surface and mobilize toward the central marrow as they differentiate in BM. In addition, SRC-enriched CD34+CD38− cells demonstrated a distinct trend to localize in the endosteal region and to interact with bone-lining osteoblasts, even at the early stage of hematopoietic reconstitution. This may be one of the reasons that CD34+CD38− cells have the high repopulation potential. We also found that human MSC-derived HMRCs locally created human HME in the murine environment. Visualization of human hematopoietic cells and human HMRCs in situ made it possible to elucidate the physical interaction between human hematopoietic cells and the human microenvironment. In this way, the SRC assay recapitulates human hematopoiesis in the murine environment both structurally and functionally and could serve as a good experimental system to study human hematopoiesis.

The presence of human MSCs in murine BM resulted in significantly more engraftment of phenotypically and functionally primitive human hematopoietic cells. With this newly established experimental system, we were able to present 3 lines of evidence that explain how human MSCs may facilitate human hematopoietic cell engraftment. First, the interaction of human MSC-derived HMRCs and human CD34+ cells was mostly observed in the
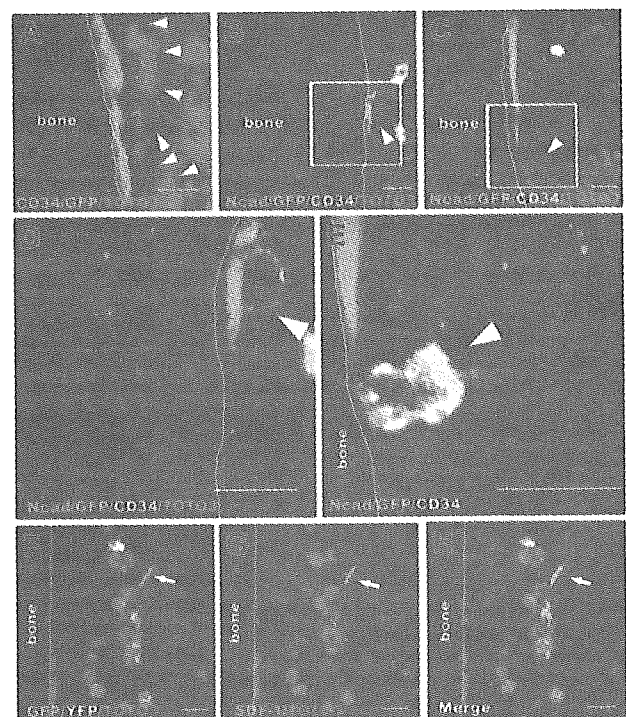
Figure 7. Expression of N-cadherin and SDF-1 by HMRCs that interact with human hematopoietic cells. (A) CD34+ cells (arrowheads) appear to colonize near the bone-lining HMRCs. (B-C) Bone-lining HMRCs colocalize with CD34+ cells (arrowheads) through the asymmetrical expression of N-cadherin. (D-E) Higher magnifications of panels B and C. (F-H) An HMRC in the endosteal hematopoietic parenchyma (arrow) expresses SDF-1 and interacts with a few eYFP hematopoietic cells. All bars represent 10 μm.

endosteal region, at a significantly higher frequency than that of lineage-committed cells. When this interaction was examined further by using sorted populations of SRC-enriched CD34+CD38− cells and more mature CD34+CD38+ progenitor cells, a preferential interaction of HMRCs with a primitive population of CD34+ cells was evident. Whereas the proportion of CD34+ cells interacting with HMRCs rapidly decreased in the group that had received CD34+CD38+ progenitor cells, this frequency in the group that had received CD34+CD38− transplants did not change and was equivalent to the proportion of CD34+ cells interacting with HMRCs at 10 weeks after transplantation. Considering that the proportion of CD34+CD38− cells originally contained in the CD34+ cells (representing 5%-8% of CD34+ cells in this study) was similar to HMRC-interacting CD34+ cells (8.0% ± 6.2% at 10 weeks), transplanted human MSCs, which became an integral part of the functional HME, interacted with primitive cell populations, provided supportive environment of human hematopoiesis, and augmented human cell engraftment. Second, bone-lining HMRCs interacted with CD34+ cells through the asymmetric expression of N-cadherin, similar to the way bone-lining osteoblasts maintain primitive HSCs in mouse. This specific interaction of CD34+ cells with human MSC-derived bone-lining osteoblasts, a cellular component of the stem cell niche, indicates that similar regulatory mechanisms operate in human and murine hematopoiesis. Third, HMRCs in the endosteal hematopoietic parenchyma produced SDF-1 and interacted with human hematopoietic cells. This strengthens the previous observations that SDF-1 regulates the proliferation and survival of primitive HSCs and progenitor cells.[12,42-44] Taken together, these results suggest that human MSC-derived HMRCs contribute not only to the proliferation and differentiation of human hematopoietic progenitor cells that results in the increased chimerism but also to the maintenance of primitive human HSCs.

Embryonic development is strictly regulated through sequential and concerted events that are orchestrated by interactions between tissue stem cells and the microenvironment. This developmental paradigm, including signaling molecules that regulate stem cell self-renewal,[49] is conserved for generating and maintaining specific tissues in adult life, and dysregulation of this process leads to pathologic conditions such as cancer.[50] Current empiric cancer studies have focused on identifying intrinsic genetic changes that lead to the aberrant proliferation of cells, and, as a result, therapeutic agents targeting the genetic mutations are emerging. However, our understanding of extrinsic, or microenvironmental, signals in the context of tumorigenesis has lagged behind. Because the microenvironment is responsible for homeostatic controls,[45,51,52] is there a specific microenvironment that permits, initiates, or complements tumorigenesis and supports progression of tumors? Could the microenvironment be a new target for cancer therapy? The experimental system we described here, which allows the visualization and reconstitution of a human microenvironment, provides a unique tool to study the maintenance of tissue homeostasis, which may lead to the elucidation of the tumorigenic microenvironment. In addition, the functional persistence of transplanted MSCs in the host environment means that MSCs may be used to deliver therapeutic genes or agents to target tissues.

References

1. Prockop DJ. Marrow stromal cells as stem cells for nonhematopoietic tissues. Science. 1997;276: 71-74.

2. Pittenger MF, Mackay AM, Beck SC, et al. Multilineage potential of adult human mesenchymal stem cells. Science. 1999;284:143-147.

3. Conget PA, Minguell JJ. Phenotypical and functional properties of human bone marrow mesenchymal progenitor cells. J Cell Physiol. 1999;181: 67-73.

4. Majumdar MK, Thiede MA, Mosca JD, Moorman M, Gerson SL. Phenotypic and functional comparison of cultures of marrow-derived mesenchymal stem cells (MSCs) and stromal cells. J Cell Physiol. 1998;176:57-66.

5. Javazon EH, Beggs KJ, Flake AW. Mesenchymal stem cells: paradoxes of passaging. Exp Hematol. 2004;32:414-425.

6. Koc ON, Gerson SL, Cooper BW, et al. Rapid hematopoietic recovery after coinfusion of autologous-blood stem cells and culture-expanded marrow mesenchymal stem cells in advanced breast cancer patients receiving high-dose chemotherapy. J Clin Oncol. 2000;18:307-316.

7. Noort WA, Kruisselbrink AB, in 't Anker PS, et al. Mesenchymal stem cells promote engraftment of human umbilical cord blood-derived CD34(+) cells in NOD/SCID mice. Exp Hematol. 2002;30: 870-878.

8. In 't Anker PS, Noort WA, Kruisselbrink AB, et al. Nonexpanded primary lung and bone marrow-derived mesenchymal cells promote the engraftment of umbilical cord blood-derived CD34(+) cells in NOD/SCID mice. Exp Hematol. 2003;31: 881-889.

9. Bensidhoum M, Chapel A, Francois S, et al. Homing of in vitro expanded Stro-1− or Stro-1+ human mesenchymal stem cells into the NOD/SCID mouse and their role in supporting human CD34 cell engraftment. Blood. 2004;103:3313-3319.

10. Devine SM, Bartholomew AM, Mahmud N, et al. Mesenchymal stem cells are capable of homing to the bone marrow of non-human primates following systemic infusion. Exp Hematol. 2001;29: 244-255.

11. Awaya N, Rupert K, Bryant E, Torok-Storb B. Failure of adult marrow-derived stem cells to generate marrow stroma after successful hematopoietic stem cell transplantation. Exp Hematol. 2002; 30:937-942.

12. Yahata T, Ando K, Sato T, et al. A highly sensitive strategy for SCID-repopulating cell assay by direct injection of primitive human hematopoietic cells into NOD/SCID mice bone marrow. Blood. 2003;101:2905-2913.

13. Wang J, Kimura T, Asada R, et al. SCID-repopulating cell activity of human cord blood-derived CD34- cells assured by intra-bone marrow injection. Blood. 2003; 101:2924-2931.

14. Kawada H, Fujita J, Kinjo K, et al. Nonhematopoietic mesenchymal stem cells can be mobilized and differentiate into cardiomyocytes after myocardial infarction. Blood. 2004;104:3581-3587.

15. Yahata T, Ando K, Miyatake H, et al. Competitive repopulation assay of two gene-marked cord blood units in NOD/SCID/gammac(null) mice. Mol Ther. 2004;10:882-891.

16. Muguruma Y, Reyes M, Nakamura Y, et al. In vivo and in vitro differentiation of myocytes from human bone marrow-derived multipotent progenitor cells. Exp Hematol. 2003;31:1323-1330.

17. Yahata T, Ando K, Nakamura Y, et al. Functional human T lymphocyte development from cord blood CD34+ cells in nonobese diabetic/Shi-scid, IL-2 receptor gamma null mice. J Immunol. 2002; 169:204-209.

18. Ito M, Hiramatsu H, Kobayashi K, et al. NOD/SCID/gamma(c)(null) mouse: an excellent recipient mouse model for engraftment of human cells. Blood. 2002;100:3175-3182.

19. Nilsson SK, Johnston HM, Coverdale JA. Spatial localization of transplanted hemopoietic stem cells: inferences for the localization of stem cell niches. Blood. 2001;97:2293-2299.

20. Larochelle A, Vormoor J, Hanenberg H, et al. Identification of primitive human hematopoietic cells capable of repopulating NOD/SCID mouse bone marrow: implications for gene therapy. Nat Med. 1996;2:1329-1337.

21. Lambertsen RH, Weiss L. A model of intramedullary hematopoietic microenvironments based on

stereologic study of the distribution of endocloned marrow colonies. Blood. 1984;63:287-297.

22. Heissig B, Hattori K, Dias S, et al. Recruitment of stem and progenitor cells from the bone marrow niche requires MMP-9 mediated release of kit-ligand. Cell. 2002;109:625-637.

23. Peled A, Zipori D, Abramsky O, Ovadia H, Shezen E. Expression of alpha-smooth muscle actin in murine bone marrow stromal cells. Blood. 1991;78:304-309.

24. Charbord P, Tavian M, Humeau L, Peault B. Early ontogeny of the human marrow from long bones: an immunohistochemical study of hematopoiesis and its microenvironment. Blood. 1996;87:4109-4119.

25. Westen H, Bainton DF. Association of alkaline-phosphatase-positive reticulum cells in bone marrow with granulocytic precursors. J Exp Med. 1979;150:919-937.

26. Lichtman MA. The ultrastructure of the hemopoietic environment of the marrow: a review. Exp Hematol. 1981;9:391-410.

27. Pereira RF, O'Hara MD, Laptev AV, et al. Marrow stromal cells as a source of progenitor cells for nonhematopoietic tissues in transgenic mice with a phenotype of osteogenesis imperfecta. Proc Natl Acad Sci U S A. 1998;95:1142-1147.

28. Nilsson SK, Dooner MS, Weier HU, et al. Cells capable of bone production engraft from whole bone marrow transplants in nonablated mice. J Exp Med. 1999;189:729-734.

29. Zhang J, Niu C, Ye L, et al. Identification of the haematopoietic stem cell niche and control of the niche size. Nature. 2003;425:836-841.

30. Calvi LM, Adams GB, Weibrecht KW, et al. Osteoblastic cells regulate the haematopoietic stem cell niche. Nature. 2003;425:841-846.

31. Arai F, Hirao A, Ohmura M, et al. Tie2/angiopoietin-1 signaling regulates hematopoietic stem cell quiescence in the bone marrow niche. Cell. 2004; 118:149-161.

32. Visnjic D, Kalajzic Z, Rowe DW, Katavic V, Lorenzo J, Aguila HL. Hematopoiesis is severely altered in mice with an induced osteoblast deficiency. Blood. 2004;103:3258-3264.

33. Stier S, Ko Y, Forkert R, et al. Osteopontin is a hematopoietic stem cell niche component that negatively regulates stem cell pool size. J Exp Med. 2005;201:1781-1791.

34. Nilsson SK, Johnston HM, Whitty GA, et al. Osteopontin, a key component of the hematopoietic stem cell niche and regulator of primitive hematopoietic progenitor cells. Blood. 2005;106:1232-1239.

35. Terstappen LW, Huang S, Safford M, Lansdorp PM, Loken MR. Sequential generations of hematopoietic colonies derived from single nonlineage-committed CD34$^+$CD38$^-$ progenitor cells. Blood. 1991;77:1218-1227.

36. Craig W, Kay R, Cutler RL, Lansdorp PM. Expression of Thy-1 on human hematopoietic progenitor cells. J Exp Med. 1993;177:1331-1342.

37. Yin AH, Miraglia S, Zanjani ED, et al. AC133, a novel marker for human hematopoietic stem and progenitor cells. Blood. 1997;90:5002-5012.

38. Baum CM, Weissman IL, Tsukamoto AS, Buckle AM, Peault B. Isolation of a candidate human hematopoietic stem-cell population. Proc Natl Acad Sci U S A. 1992;89:2804-2808.

39. Murray LJ, Bruno E, Uchida N, et al. CD109 is expressed on a subpopulation of CD34$^+$ cells enriched in hematopoietic stem and progenitor cells. Exp Hematol. 1999;27:1282-1294.

40. Ponomaryov T, Peled A, Petit I, et al. Induction of the chemokine stromal-derived factor-1 following DNA damage improves human stem cell function. J Clin Invest. 2000;106:1331-1339.

41. Lapidot T. Mechanism of human stem cell migration and repopulation of NOD/SCID and B2mnull NOD/SCID mice. The role of SDF-1/CXCR4 interactions. Ann N Y Acad Sci. 2001;938:83-95.

42. Lataillade JJ, Clay D, Dupuy C, et al. Chemokine

SDF-1 enhances circulating CD34(+) cell proliferation in synergy with cytokines: possible role in progenitor survival. Blood. 2000;95:756-768.

43. Lataillade JJ, Clay D, Bourin P, et al. Stromal cell-derived factor 1 regulates primitive hematopoiesis by suppressing apoptosis and by promoting G(0)/G(1) transition in CD34(+) cells: evidence for an autocrine/paracrine mechanism. Blood. 2002;99:1117-1129.

44. Cashman J, Clark-Lewis I, Eaves A, Eaves C. Stromal-derived factor 1 inhibits the cycling of very primitive human hematopoietic cells in vitro and in NOD/SCID mice. Blood. 2002;99:792-799.

45. Watt FM, Hogan BL. Out of Eden: stem cells and their niches. Science. 2000;287:1427-1430.

46. Spradling A, Drummond-Barbosa D, Kai T. Stem cells find their niche. Nature. 2001;414:98-104.

47. Taichman RS. Blood and bone: two tissues whose fates are intertwined to create the hematopoietic stem-cell niche. Blood. 2005;105:2631-2639.

48. Guenechea G, Gan OI, Dorrell C, Dick JE. Distinct classes of human stem cells that differ in proliferative and self-renewal potential. Nat Immunol. 2001;2:75-82.

49. Taipale J, Beachy PA. The Hedgehog and Wnt signalling pathways in cancer. Nature. 2001;411: 349-354.

50. Reya T, Morrison SJ, Clarke MF, Weissman IL. Stem cells, cancer, and cancer stem cells. Nature. 2001;414:105-111.

51. Antonchuk J, Sauvageau G, Humphries RK. HOXB4 overexpression mediates very rapid stem cell regeneration and competitive hematopoietic repopulation. Exp Hematol. 2001;29:1125-1134.

52. Mueller MM, Fusenig NE. Friends or foes—bipolar effects of the tumour stroma in cancer. Nat Rev Cancer. 2004;4:839-849.

Efficient intervention of growth and infiltration of primary adult T-cell leukemia cells by an HIV protease inhibitor, ritonavir

M. Zahidunnabi Dewan, Jun-nosuke Uchihara, Kazuo Terashima, Mitsuo Honda, Tetsutaro Sata, Mamoru Ito, Nobutaka Fujii,
Kimiharu Uozumi, Kunihiro Tsukasaki, Masao Tomonaga, Yoko Kubuki, Akihiko Okayama, Masakazu Toi, Naoki Mori, and Naoki Yamamoto

Adult T-cell leukemia (ATL), an aggressive malignancy of CD4^{+} T cells associated with human T-cell leukemia virus type I (HTLV-I) infection, carries a very poor prognosis because of the resistance of leukemic cells to any conventional regimen, including chemotherapy. We examined the effect of ritonavir, an HIV protease inhibitor, on HTLV-I–infected T-cell lines and primary ATL cells and found that it induced apoptosis and inhibited transcriptional activation of NF-κB in these cells. Furthermore, ritonavir inhibited expression of Bcl-x_L, survivin, c-Myc, and cyclin D2, the targets of NF-κB. In nonobese diabetic/severe combined immunodeficient (NOD/SCID)/γc^{null} (NOG) mice, ritonavir very efficiently prevented tumor growth and leukemic infiltration in various organs of NOG mice at the same dose used for treatment of patients with AIDS. Our data indicate that ritonavir has potent anti–NF-κB and antitumor effects and might be clinically applicable for treatment of ATL. These results would provide a new concept and novel platform for new drug development of leukemia and solid cancer as well. (Blood. 2006;107:716-724)

© 2006 by The American Society of Hematology

Introduction

Human T-cell leukemia virus type I (HTLV-I) is the causative agent of an aggressive form of CD4^{+} T-cell leukemia designated adult T-cell leukemia (ATL).[1-3] ATL was first identified in Japan in 1977.[4,5] Common findings for patients with ATL include enlargement of peripheral lymph nodes, hepatomegaly, splenomegaly, hypercalcemia, and skin lesions. At present, there is no accepted curative therapy for ATL, and patients progress to death with a median survival duration of 13 months in aggressive ATL.[6] ATL has a poor prognosis mainly because of its resistance to conventional as well as high-dose chemotherapy.

ATL develops after a long period of latent infection. This long latency suggests that multiple genetic events, which accumulate in HTLV-I–infected cells, are involved in the development of ATL. However, the precise molecular mechanism of leukemogenesis and the development of ATL after HTLV-I infection are not fully elucidated. A unique viral gene Tax is considered to play a central role in HTLV-I–induced transformation, which is responsible for transactivation of the HTLV-I long terminal repeat,[7,8] as well as numerous cellular genes involved in T-cell activation and growth, such as those encoding IL-2,[9] and the α-chain of IL-2 receptor

(IL-2Rα) (CD25, Tac).[10,11] Induction of many cellular genes by Tax is mediated through the transcription factor NF-κB. The malignant cells associated with all phases of ATL express very high levels of IL-2Rα[12-14] without expressing a significant amount of Tax.

HTLV-I–infected cell lines derived from a leukemic cell clone and primary ATL cells failed to express significant amounts of Tax and other viral proteins, suggesting that the expression of viral proteins is not always necessary for leukemic proliferation at the late stage of the disease. However, HTLV-I–infected cell lines and leukemic cells from patients with ATL display constitutive NF-κB binding activity and increased degradation of a specific inhibitor, IκBα.[15] In resting cells, NF-κB is sequestered as an inactive precursor by association with inhibitory IκBs in the cytoplasm. On stimulation, IκBs are rapidly phosphorylated, ubiquitinated, and degraded by a proteasome-dependent pathway, allowing active NF-κB to translocate into the nucleus where it can activate the expression of a number of genes.[16] NF-κB activation has been connected with multiple processes of oncogenesis, including control of apoptosis, cell cycle, differentiation, and cell migration[16]; therefore, inhibition of NF-κB was suggested to be a useful

strategy for cancer therapy.[17-20] Despite the diversity in clinical manifestations of ATL, strong and constitutive NF-κB activation was reported to be a unique and common characteristic of ATL cells.[15] Thus, the indispensability of NF-κB for the maintenance of the malignant phenotype of HTLV-I provides a possible molecular target for ATL therapy.[21-24]

Ritonavir, a human immunodeficiency virus type 1 (HIV-1) protease inhibitor (PI), has been successfully used in clinical treatments of HIV infection, with patients exhibiting a marked decrease in HIV viral load and a subsequent increase in CD4⁺ T-cell counts.[25-28] Evidence of other effects by ritonavir on cellular proteases, such as the cysteine proteases cathepsin D and E, was presented in the drug's original description, albeit at concentrations greater than 500-fold above the concentration required for inhibition of HIV protease.[29] PIs have also been shown to directly affect cell metabolism, interfere with host or fungal proteases, and block T-cell activation and dendritic cell function.[30,31] Recently, ritonavir has been shown to inhibit the chymotrypsin-like activity of the 20S proteasome, and it activates the chymotrypsin-like activity of the 26S proteasome conversely.[30,32,33] Ritonavir also has been reported to inhibit the transactivation of NF-κB induced by activators such as TNFα, HIV-1 Tat protein, and the human herpesvirus 8 protein ORF74. It is possible that inhibition of NF-κB activation by ritonavir is linked to additional pathways other than inhibition of proteasome.[34] PIs also have been shown to have direct antiangiogenic and antitumor activity[34,35]

In this study, we investigated the antitumor effects of ritonavir on HTLV-I–infected cell lines and primary ATL cells. We found that ritonavir decreases NF-κB activity linked to the inhibition of IκBα phosphorylation and induces apoptosis of these cells. In addition, we established preclinical models to evaluate the efficacy of anti-ATL and anti–NF-κB therapies. In the ATL model, ritonavir potently inhibited the growth and infiltration of leukemic cells from patients at concentrations used for treatment of patients with AIDS.

Materials and methods

Cell lines

The T-cell leukemia cell line Jurkat, HTLV-I–infected T-cell lines MT-2,[36] MT-4,[37] C5/MJ,[38] SLB-1,[39] HUT-102,[2] MT-1,[40] and ED-40515(−),[41] and bcr-abl⁺ leukemic cell line K562 were cultured in RPMI 1640 medium supplemented with 2% heat-inactivated fetal bovine serum (JRH Biosciences, Lenexa, KS), 100 U/mL penicillin, and 10 μg/mL streptomycin. MT-2, MT-4, C5/MJ, and SLB-1 are HTLV-I–transformed T-cell lines. MT-1 and ED-40515(−) are T-cell lines of leukemic cell origin established from patients with ATL. The clonal origin of HUT-102 is unclear.

Human specimens

Leukemic cells from 38 patients (8 patient samples for in vitro studies, 20 for establishment of ATL model, 10 for in vivo ritonavir studies) diagnosed as either acute type or chronic type were used in this study. The diagnosis of ATL was based on clinical features, hematologic findings, and the presence of anti–HTLV-I antibodies in the sera. Baseline characteristics for the patients who entered the study are shown in Table 1. Monoclonal HTLV-I provirus integration into the DNA of leukemia cells was confirmed by Southern blot hybridization in all cases (data not shown). All samples were collected after obtaining informed consent from patients. Peripheral blood mononuclear cells (PBMCs) from healthy volunteers and patients with ATL were purified by Ficoll-Hypaque gradient centrifugation (Amersham Biosciences, Uppsala, Sweden) and washed with RPMI 1640.

Growth inhibition assay

The effect of ritonavir on cell growth was assayed by the WST-8 method as described previously.[42] The WST-8 Cell Counting Kit was obtained from Wako Chemicals (Osaka, Japan). Briefly, 2 × 10⁵ cells were incubated in a 96-well microculture plate in the absence or presence of various concentrations of ritonavir. After 72 hours of culture, 10 μL WST-8 solution was added, and the cells were incubated for another 2 hours. The number of surviving cells was measured with a microplate reader at a reference wavelength of 655 nm and test wavelength of 450 nm. Cell viability was determined as the percentage of the control (ie, absence of ritonavir).

Assay for apoptosis

Quantification of apoptosis was performed by immunostaining cells with Apo2.7, which specifically detects the 38-kDa mitochondrial membrane antigen 7A6 present only on the mitochondrial membrane of apoptotic cells, and so can be used as an early apoptotic marker in cells.[43,44] Cells cultured for 72 hours in the absence or presence of various concentrations of ritonavir were labeled with the Apo2.7-phycoerythrin–conjugated monoclonal antibody (Beckman-Coulter/Immunotech, Miami, Florida) or mouse IgG1 isotype control (Beckman-Coulter/Immunotech) and subsequently analyzed by flow cytometry.

EMSA

Cells were placed in culture at 1 × 10⁶ cells/mL (cell line) or 5 × 10⁶ cells/mL (PBMCs) and examined for inhibition of NF-κB after exposure to ritonavir. Nuclear proteins were extracted, and NF-κB binding activities to κB element were examined by electrophoretic mobility shift assay (EMSA) as described previously.[15] In brief, 5 μg nuclear extracts were preincubated in a binding buffer containing 1 μg poly(dI:dC) (Amersham Biosciences), followed by addition of ³²P-labeled oligonucleotide probe containing NF-κB element (5 × 10⁴ cpm). These mixtures were incubated for 15 minutes at room temperature. The DNA-protein complexes were separated on a 4% polyacrylamide gel and visualized by autoradiography. To examine the specificity of the NF-κB element probe, unlabeled competitor oligonucleotides were preincubated with nuclear extracts for 15 minutes before incubation with probes. The probe or competitors used were prepared by annealing the sense and antisense synthetic oligonucleotides as follows: a typical NF-κB element from the *IL2RA* gene, 5′-gatcCGGCAGGG-GAATCTCCCTCTC-3′; and AP-1 element of the *IL8* gene, 5′-gatcGTGAT-GACTCAGGTT-3′. Underlined sequences represent the NF-κB or AP-1 binding site. To identify NF-κB proteins in the DNA protein complex revealed by EMSA, we used antibodies specific for various NF-κB proteins, including p65, p50, c-Rel, and p52 (Santa Cruz Biotechnology, Santa Cruz, CA), to elicit a supershift DNA protein complex formation. These antibodies were incubated with the nuclear extracts for 45 minutes at room temperature before incubation with radiolabeled probes.

Western blot analysis

Treated cells were solubilized at 4°C in lysis buffer containing 62.5 mM Tris-HCl (pH 6.8), 2% SDS, 10% glycerol, 6% 2-mercaptoethanol, and 0.01% bromophenol blue. Samples were subjected to electrophoresis on SDS-polyacrylamide gels followed by transfer to a polyvinylidene difluoride membrane and probing with the following specific antibodies: polyclonal antibodies against IκBα, cIAP2, survivin, cyclin D2 (Santa Cruz Biotechnology), Bcl-XL (Transduction Laboratories, San Jose, CA), and c-Myc (NeoMarkers, Fremont, CA) and monoclonal antibodies against phospho-IκBα, hyperphosphorylated form of pRb (Cell Signaling Technology, Beverly, MA), Bcl-2, and actin (NeoMarkers). The protein bands recognized by the antibodies were visualized using the enhanced chemiluminescence system (Amersham, Piscataway, NJ).

Plasmids and transfection

Reporter plasmid κB-LUC (kindly provided by J. Fujisawa, Kansai Medical University, Osaka, Japan) is a luciferase expression plasmid controlled by 5 tandem repeats of a NF-κB binding site from the *IL2RA*

Table 1. Clinical characteristics of patients

Patient	Age, y/sex	Diagnosis	WBC count, cells × 10⁹/L	Lymphocytes, %	Atypical cells, %	Treatment status
1	54/M	Acute	192.80	65.0	91.0	Untreated
2	77/F	Acute	186.0	41.0	70.0	Untreated
3	67/F	Chronic	10.40	38.0	89.0	Treated
4	58/M	Acute	67.30	71.0	80.0	Treated
5	71/M	Acute	19.70	51.0	61.0	Treated
6	66/F	Chronic	29.40	49.0	75.0	Untreated
7	48/F	Chronic	9.40	29.0	55.0	Untreated
8	69/F	Acute	53.80	44.0	95.0	Treated
9	58/M	Chronic	11.30	59.0	70.0	Treated
10	60/M	Chronic	9.12	61.0	80.0	Treated
11	65/F	Acute	29.40	25.0	60.0	Untreated
12	49/F	Chronic	15.10	48.0	75.0	Treated
13	57/M	Chronic	10.00	50.0	57.0	Treated
14	72/F	Acute	39.00	70.0	80.0	Treated
15	79/F	Chronic	10.10	47.0	27.0	Untreated
16	68/F	Acute	7.00	86.0	86.0	Treated
17	59/F	Chronic	8.99	74.5	40.0	Treated
18	70/M	Acute	31.60	71.7	68.0	Treated
19	49/M	Acute	5.00	19.5	78.0	Treated
20	44/M	Chronic	36.40	33.0	43.0	Untreated
21	65/F	Chronic	14.70	76.0	22.0	Untreated
22	63/F	Acute	12.40	71.0	82.0	Untreated
23	56/F	Chronic	7.20	46.0	15.0	Treated
24	78/F	Acute	94.50	63.3	49.0	Treated
25	62/F	Acute	10.10	53.0	27.0	Untreated
26	66/M	Chronic	38.10	63.0	39.0	Treated
26	39/F	Chronic	18.50	16.0	57.0	Untreated
28	48/F	Acute	53.50	39.0	64.0	Untreated
29	75/F	Acute	15.00	72.0	65.0	Untreated
30	84/F	Acute	14.40	69.0	61.0	Treated
31	73/M	Chronic	7.80	59.0	47.0	Untreated
32	43/F	Chronic	18.60	63.0	43.0	Untreated
33	54/F	Acute	69.00	49.0	50.0	Untreated
34	66/F	Acute	10.20	38.0	51.0	Untreated
35	73/F	Chronic	15.70	58.0	39.0	Untreated
36	63/F	Acute	32.90	71.0	95.0	Treated
37	44/F	Chronic	22.60	51.0	45.0	Untreated
38	68/M	Acute	30.00	79.0	81.0	Untreated

WBC indicates white blood cells.

gene. Reporter plasmid AP-1–LUC (kindly provided by N. Mukaida, Kanazawa University, Kanazawa, Japan) is a luciferase expression plasmid controlled by 2 copies of the AP-1 binding site from the IL-8 promoter. The expression plasmid for HTLV-I Tax has been described previously.[45] Transient transfections were performed in Jurkat and HUT-102 cells by electroporation using 5×10^6 cells and reporter and effecter plasmids. To normalize transfection efficiencies, a thymidine kinase (TK) promoter-driven Renilla luciferase plasmid (phRL-TK; Promega, Madison, WI) was cotransfected as an internal control plasmid. Then, 16 hours after transfection, ritonavir was added to the cultures at various concentrations, and cells were further cultured for 24 hours for assay of luciferase activity. Transfected cells were collected by centrifugation, washed with phosphate-buffer saline (PBS), and lysed in reporter lysis buffer (Promega). Lysates were assayed for reporter gene activity with the dual-luciferase reporter assay system (Promega).

Inoculation of ATL cells and collection of samples

NOG mice were obtained from the Central Institute for Experimental Animals (Kawasaki, Japan). All mice were maintained under specific pathogen-free conditions in the Animal Center of National Institute of Infectious Diseases (Tokyo, Japan). The Ethical Review Committee of the Institute approved the experimental protocol. Mice were anesthetized with ether, and cells were inoculated either intraperitoneally in

abdominal region or subcutaneously in the postauricular region of NOG mice without injection of human recombinant IL-2 at a dose of 1 to 2×10^7 cells per mouse. All mice were killed 30 or 60 days after inoculation with primary ATL cells. Blood was collected from the tail to make a smear, as well as from the heart with heparinized syringes. PBMCs and splenocytes were isolated by density gradient concentration with Ficoll-Hypaque. Blood smear slides were fixed in methyl alcohol for May-Grunwald and Giemsa staining. PBMCs and splenocytes were stored at −80°C for further experiments. Tissues and various organs of mice were collected and fixed with Streck Tissue Fixative, then processed to paraffin wax-embedded sections for staining with hematoxylin and eosin (HE) and immunostaining.

Treatment of ATL mice with ritonavir

Ritonavir was obtained from Abbott Labs, North Chicago, IL. Primary ATL cells (2×10^7) from 10 patients were inoculated subcutaneously in the postauricular region of NOG mice. One day after inoculation of ATL cells, mice were treated with either RPMI 1640 (control mice) or drug (ritonavir 30 mg/kg/d) intraperitoneally daily for 30 days followed by observation for another 30 days without treatment. ATL cell growth and progression were monitored by observation of physical condition of mice during a 2-month follow-up period.

Immunohistochemistry

Paraffinized cryosections of various organs were deparaffinized and hydrated in xylenes or clearing agents and graded alcohol series, then rinsed for 5 minutes in water. Deparaffinized samples were incubated with 0.025% trypsin/PBS for 30 minutes followed by washing, and then incubated with 0.3% methanol for 30 minutes at room temperature and washed 2 times with PBS. Immunostaining was done as described previously[46] using Vector MOM immunodetection kit (Vector Labs, Burlingame CA) for ATL cells with a 1:500 dilution of primary mouse monoclonal antibody specific for human CD4 and CD25 (Dako, Caterpillar, CA). This was followed by washing in PBS and incubation with a secondary antibody MOM biotinylated anti–mouse IgG, after which cells were again washed in PBS and incubated with VECTASTAIN *Elite* ABC for 20 minutes at room temperature. Positive staining was visualized after incubation of these samples with a mixture of 0.05% 3,3'-diaminobenzidine tetrahydrochloride in 50 mM Tris-HCl buffer and 0.01% hydrogen peroxide for 5 minutes. The samples were counterstained with hematoxylin for 2 minutes, hydrated completely, cleaned in xylene, and then mounted. Photographs were taken by light microscopy (BX41, Olympus, Tokyo, Japan) using UplanF1 lenses (DP70, Olympus; magnification ×40).

Results

Ritonavir reduces cell growth and induces apoptosis of HTLV-I–infected cell lines and primary ATL cells

Ritonavir was examined for its effect on proliferation of HTLV-I–infected cell lines (Figure 1A). Ritonavir effectively inhibited the proliferation of HTLV-I–infected cell lines as measured by WST-8 on the third day of culture in a dose-dependent manner, but not that of K562 cells. Further experiments using Apo2.7 showed that ritonavir caused apoptosis of HTLV-I–infected cell lines in a dose-dependent manner, but not that of K562 cells (Figure 1B-C). In addition, we explored the anti-ATL effect of ritonavir on freshly isolated ATL cells from patients. In all ATL cases, ritonavir reduced the survival of ATL cells in a dose-dependent manner (Figure 1D). Ritonavir also caused apoptosis of ATL cells (Figure 1E). In contrast, ritonavir hardly affected the survival of peripheral blood mononuclear cells (PBMCs) from 3 healthy volunteers as measured by WST-8 (Figure 1D).

Ritonavir suppresses constitutive NF-κB expressed by HTLV-I–infected cell lines and primary ATL cells

To examine the effect of ritonavir on NF-κB DNA binding, electrophoretic mobility shift assay (EMSA) was performed. We first examined the minimum duration of exposure to ritonavir required for suppression of NF-κB. For this, HUT-102 cells were incubated with 40 μM ritonavir for different periods of time, and nuclear extracts were prepared and examined for NF-κB by EMSA. Down-regulation of NF-κB occurred at 24 hours in HUT-102 cells. However, no change in binding activity of AP-1 was observed (Figure 2A). The observed protein/DNA binding was specific for NF-κB, because the binding was effectively competed and abrogated by excess unlabeled NF-κB oligonucleotide but not by AP-1 (Figure 2C). The NF-κB complex contained p50, p65, and c-Rel (Figure 2C). Forty micromolar concentration of ritonavir was sufficient to suppress constitutive NF-κB activation in residual HTLV-I–infected T-cell lines (data not shown). It should be noted that K562 cells did not show constitutive NF-κB activation (data not shown). We also found a concentration-dependent inhibitory effect of ritonavir on the constitutive increase of NF-κB DNA binding activity (Figure 2B). Twenty micromolar concentration of
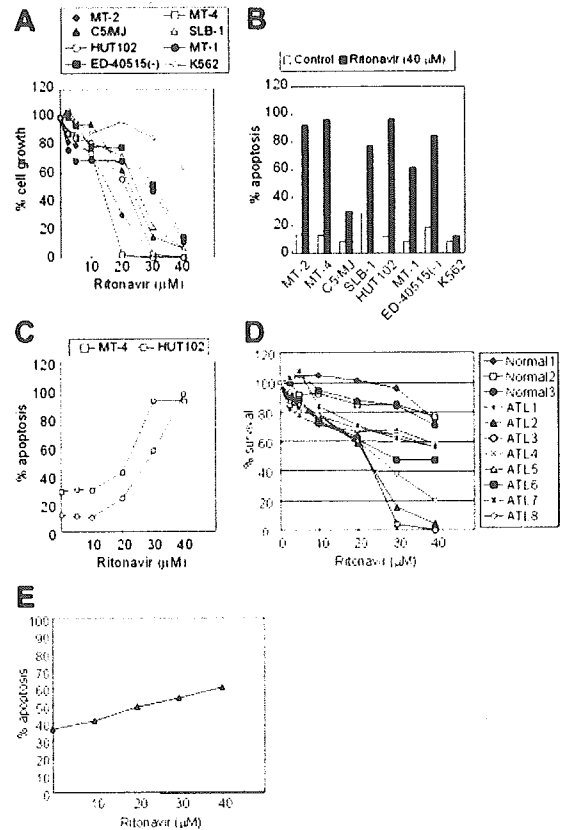
Figure 1. Effect of ritonavir on the growth and induction of apoptosis of HTLV-I–infected cell lines and freshly isolated ATL cells. (A) Dose-response effect of ritonavir on the growth of HTLV-I–infected cell lines. Cells (10⁵/mL) were cultured for 72 hours in the presence of various concentrations (2.5-40 μM) of ritonavir. Cell growth was assessed by the water-soluble tetrazolium (WST)-8 method and is expressed as a percentage of control (untreated cells) and represents the mean of triplicate cultures. (B) Effect of ritonavir on induction of apoptosis of HTLV-I–infected cell lines. Cells were cultured for 72 hours with ritonavir (40 μM), and apoptosis was measured by Apo2.7 immunostaining. Data represent the mean percentages of apoptotic cells from both untreated (□) and ritonavir-treated (■) cells. (C) Dose-response effect of ritonavir on induction of apoptosis of MT-4 and HUT-102 cells. (D) Dose-response effect of ritonavir on the cell viability of freshly isolated ATL cells. Cells (10⁶/mL) were cultured for 72 hours in the presence of various concentrations (2.5-40 μM) of ritonavir. (E) Dose-response effect of ritonavir on induction of apoptosis of ATL cells.

ritonavir caused only a partial inhibition of NF-κB/DNA binding, whereas strong inhibition was observed at 30 and 40 μM in HUT-102 cells. However, AP-1 binding was not inhibited. This inhibition coincided with an accumulation of unphosphorylated IκBα and a decrease of the slower-migrating form of phosphorylated IκBα, a prerequisite for its subsequent degradation (Figure 2D, top). Thirty micromolar concentration of ritonavir caused only a partial decrease of the slower-migrating form of phosphorylated IκBα, whereas significant decrease of the slower-migrating form of phosphorylated IκBα and an accumulation of unphosphorylated IκBα were observed at 40 μM. We determined the alteration of phosphorylation of IκBα using antibody against phosphospecific IκBα. Results in Figure 2D (middle) show that 40 μM ritonavir decreased the phosphorylated IκBα content. We also determined whether the same results were obtained in primary ex vivo ATL specimens. As shown in Figure 2E, the amount of NF-κB that translocates to the nucleus is also decreased, as determined by EMSA. Twenty micromolar concentration of ritonavir caused only a partial inhibition of NF-κB/DNA binding, whereas strong inhibition was observed at 30 μM in primary ATL cells from acute